Analytical and Numerical Models for Wind and Seismic Design and Assessment of Mass Timber Diaphragms

Leonardo G. Rodrigues[1], Andre R. Barbosa[2], Arijit Sinha[3], Christopher Higgins[4], Scott Breneman[5], Reid B. Zimmerman[6], Shiling Pei[7], John W. van de Lindt[8], Jeffrey Berman[9], Jorge M.Branco[10], and Luís A.C. Neves[11]

[1]Postdoctoral Researcher, Faculty of Engineering, University of Nottingham, UK

[2]Glenn Willis Holcomb Professor in Structural Engineering, School of Civil and Construction Engineering, Oregon State Univ., USA, andre.barbosa@oregonstate.edu

[3]Professor, Wood Science and Engineering, Oregon State Univ., USA

[4]Professor, School of Civil and Construction Engineering, Oregon State Univ., USA

[5]Senior Technical Director, WoodWorks-Wood Products Council

[6]Technical Director, KPFF Consulting Engineers, USA

[7]Associate Professor, Colorado School of Mines, USA

[8]Professor, Department of Civil and Environmental Engineering, Colorado State University, USA

[9]Professor, Department of Civil and Environmental Engineering, University of Washington, USA

[10]Assistant Professor, Department of Civil Engineering, University of Minho, Portugal

[11]Associate Professor, Faculty of Engineering, University of Nottingham, UK

Manuscript No.: Submitted to Journal of Structural Engineering

ABSTRACT

While the use of cross-laminated timber (CLT) panels for building construction has increased over the last several decades, current standards and existing literature provide limited information regarding the design of CLT diaphragms or the prediction of their deflections when subjected to wind and strong earthquake motions. This paper presents the design and assessment of a CLT diaphragm that was part of a full-scale two-story structure subjected to shake-table testing. An analytical model is proposed for diaphragm deflection accounting for in-plane shear and bending stiffness, as well as the stiffness of various connections. Moreover, a refined numerical modeling strategy is proposed in order to consider phenomena such as panel-to-panel gap closure. Results indicate that the analytical model yields conservative results both in terms of deflections and forces, when compared to the numerical model that simulates similar sources of strength and stiffness. The analytical model is suitable for the design of symmetric diaphragms with regular shapes, whereas the numerical model can also be used to model asymmetric diaphragms with an irregular shape.

CE Database: cross-laminated timber, diaphragms, mass timber, numerical modeling, seismic response, shake-table;

1. INTRODUCTION

While the use of cross-laminated timber (CLT) panels for building construction has increased over the last decades due to their construction efficiency, low environmental impacts, and aesthetics (Pei et al. 2016; Harte 2017), a large body of research has focused on supporting the development of design rules for CLT buildings in Europe (Harris et al. 2013; Thiel and Brandner 2016; Kohler et al. 2016) and, more recently, around other places in the world (Passarelli and Koshihara 2018; Li et al. 2019). In terms of structural performance, research efforts over the past 20 years in Europe, New Zealand, and North America have focused on the performance and design of lateral resisting systems (Ceccotti et al. 2006; Dujic et al. 2010; Popovski et al. 2010; van de Lindt et al. 2010; Ceccotti et al. 2013; Iqbal et al. 2015; van de Lindt et al. 2016; Sustersic et al. 2016; Ganey et al. 2017), and more specifically focusing on connections between CLT panels and other structural members. However, less attention has been given to the understanding of the performance of

CLT diaphragms (Branco et al. 2015), although some experimental testing (Hossain et al. 2016; Brandner et al. 2017; Hossain et al. 2017; Sullivan et al. 2018; Kode et al. 2021; Hossain et al. 2019; Taylor et al. 2020; Beairsto et al. 2022) has paved the way towards the development of detailed and simplified modeling tools that can be used for assessment and design of CLT diaphragms.

In design in North America, the Spickler et al. (2015) white paper covered most of the verifications needed when designing an untopped mass timber diaphragms. Spickler et al. (2015) indicated that design forces could be used under simple statics equilibrium checks and used a four-term equation for estimating deflections, which can be used to assess the flexibility of the diaphragm according to ASCE 7-16 (section 12.3.1). Despite providing an example of a diaphragm design, the white paper only considered simply supported diaphragms and did not cover other diaphragm typologies. More recently, a CLT diaphragm design guideline was developed in the US (AWC 2021), which focuses on (i) the design of panel-to-panel, chord, and collector connections assuming ductile failure modes, (ii) verification of in-plane tension, compression, and shear of CLT panels, and (iii) capacity based design of plywood surface splines and steel chord splices, through use of appropriate over-strength factors.

In New Zealand, Moroder et al. (2014) studied the behavior of timber diaphragms in multi-story timber buildings and proposed a design and assessment method that is based on an equivalent truss method. The authors suggested that the equivalent truss method could be used in the assessment of deflections of irregular mass timber diaphragms given that the deflection equation provided in the NZS 3603 design standard (Standards New Zealand 1993) is only applicable to simply supported diaphragms. However, for use in design, the results from the equivalent truss method require significant post-processing to obtain force distributions along the members. Moreover, the stiffness of diagonals depends on the spacing of fasteners and their slip modulus, and in a design process these values need to be obtained iteratively.

Numerical modeling using the finite element method can be used to analyze different loading scenarios and evaluate the response of diaphragms. Even though the construction of detailed finite element models can constitute a burdensome task that hinders their use in most design applications, most modeling approaches require modeling of the panels and their connections. Reliable high-fidelity finite element models may include shell elements modeling the panels themselves, nonlinear spring elements to represent panel-to-panel connections, springs simulating connections between panels and load-bearing elements (such as beams and walls), and springs simulating connections between supporting frames (e.g. beam-to-beam and beam-to-column connections). In terms of simulating the in-plane response of CLT panels, research performed in Gsell et al. (2007) indicated that the behavior of the panels can be modeled using a homogenized linear elastic orthotropic material. In Gsell et al. (2007), the elastic moduli of CLT panels are determined using the method proposed in Blaß and Fellmoser (2004), but there are other analytical approaches in the literature that allow the computation of in-plane shear modulus of CLT panels (Flaig and Blaß 2013; Bogensperger et al. 2010; Dröscher 2014; Brandner et al. 2017; Nairn 2019). To simulate the response of connections, a lumped springs modeling approach was developed in Breneman et al. (2016) to capture the shear transfer between panels. Breneman et al. (2016) indicated that there is a lack of guidelines for the numerical representation of the response of the chords and straps and that while promising their modeling approach required further testing results for further calibration and validation of the developed models.

Recently, D'Arenzo et al. (2019) proposed a numerical model consisting of a plane model and an equivalent frame model to capture the in-plane behavior of CLT diaphragms. The plane model proposed includes nonlinear links that represent the response of CLT-to-wall and panel-to-panel connections, while the equivalent frame model assumes the floor CLT panels as frames interconnected through translational and rotational springs. The connections of CLT panels to external CLT walls are represented by translational springs, while the connections to internal CLT walls are represented by rotational and translational springs. D'Arenzo et al. (2019) concluded that the slip between panels has a higher impact on the flexibility of the floors than panel bending. In addition, the authors concluded that the supporting walls have a strong influence on the moment distribution of the diaphragms. Despite the comprehensive and useful sensitivity analysis performed by D'Arenzo et al. (2019), the study only included diaphragms under loading applied in the direction of the panel-to-panel connections, which coincides with the major strength direction of the panels.

Based on existing knowledge, the main objective of this paper is to present numerical and analytical approaches for the design and assessment of untopped mass timber diaphragms subjected to in-plane forces due to wind or seismic loading. Diaphragms can be considered flexible, rigid, or semi-rigid and can have multiple configurations, influencing the diaphragm's distribution in-plane forces. Thus, an alternative formula is proposed for calculating deflections, given that current code provisions are mostly based on simply supported diaphragms, which do not exploit the distinct types of connections that may exist in a mass timber diaphragm. Moreover, this paper presents an analytical model based on first principles that provide a rational basis for future designs, as well as numerical models that provide insights related to different modeling assumptions and their impact on the solutions (and thereby in future designs).

The methods proposed are presented in the context of a case study application, which is presented in section 2. The case study application is a two-story mass timber floor diaphragm that was designed using the methods presented herein and then constructed and tested on the University of California San Diego (UCSD) shake-table in 2017 (Pei et al. 2019; Blomgren et al. 2019; van de Lindt et al. 2019; Barbosa et al. 2021). Given the lack of consensus on unified guidelines for the design of CLT diaphragms, the basic principles used in diaphragm design are presented first in section 3. The design strategy presented in section 3 first estimates forces on the diaphragm elements that contribute the most to the in-plane response of diaphragms, such as diaphragm chords (panel chord flexure and straps), panels, surface splines, and collectors. Section 3 also presents a five-term equation for estimating the floor diaphragm deflections under serviceability limit states (SLS) and ultimate limit states (ULS) for both wind and seismic loads, which can be seen as an alternative to the four-term equations available in Lawson et al. (2023); expressions for each of the five terms are presented generically based on the principle of virtual work and then detailed and specific equations and values are presented for the case study example in tables. Section 4 describes a numerical modeling approach that is implemented using OpenSees. Section 5 compares internal forces and peak deflections obtained using the analytical and numerical models presented in the previous sections. The integration of results from numerical models, combined with limited experimental data gathered from the two-story shake-table testing, provides a foundation for determining whether the diaphragms can be classified as either rigid or flexible. This classification is crucial for the design of vertical elements in systems that resist lateral forces.

2. DESCRIPTION OF THE CASE STUDY DIAPHRAGM

The dimensions of the floor diaphragm of the two-story mass-timber structure tested at the University of California San Diego (UCSD) outdoor shake-table are 6096 mm (20 feet) in the East-West (E-W) direction and 17700 mm (58 feet) in the North-South (N-S) direction, as shown in the plan view of Figure 1. The number and dimensions of the CLT panels are also shown; a total of sixteen (16) 3-ply CLT panels (nominally 104.8 mm thick) with their major strength direction parallel to the (N-S) direction. The CLT panels are V1 Douglas Fir grade panels per ANSI/APA PRG 320 (APA 2017), as specified in the product report of the panels used (APA 2018) . The self-tapping screws (STS) used in the diaphragms are steel grade 316, which has a minimum yield strength of 250 MPa. The surface splines constructed in panel-to-panel connections consist of 19 mm thick plywood planks fastened with partially threaded (PT) STS with a shank diameter of 5.6 mm. The gravity load-carrying system consists of glued-laminated timber (glulam) grade L2 columns and beams with grades 24F-V4 or 24F-V8 (APA 2008). The columns located at gridlines 3 and 5 have cross-section dimensions of 190.5 mm x 273.1 mm (7.5 in x 10.75 in) and the remaining columns have cross-section dimensions of 190.5 mm x 222.3 mm (7.5 in x 8.75 in). Moreover, the columns aligned with the walls on gridlines 3 and 5 are continuous, spanning two floors, while the remaining columns are interrupted at each floor level. Regarding glulam beams, two cross-sections are defined: grade 24F-V4 beams spanning the E-W direction have cross-section dimensions of 171.5 mm by 495.3 mm (6.75 in x 19.5 in), whereas the remaining 24F-V8 grade beams have a cross-section size of 222.3 mm by 495.3 mm (7.5 in x 19.5 in). The CLT panels are connected to the glulam beams using 5.6 x 200 SDWS Simpson Strong-Tie (SDWS22800 LOG) screws, as presented in Figure 1.

The analysis performed in this work is related to the structural systems tested in Phase 1 (Pei et al. 2019) and Phase 2 (Blomgren et al. 2019) of the experimental campaign, where the connection between the CLT rocking walls and the diaphragms were executed through an innovative system consisting of steel shear keys, as shown in Figure 2. These steel shear keys were restrained to the diaphragm and slotted into the walls in order to transfer the diaphragm in-plane loads to the walls. The shear keys were free to move vertically in steel slots created in the CLT wall panels, as presented in Figure 2. The shear key dimensions used in the diaphragm were 22.23 mm x 76.2 mm (5/6 in x 3.0 in), while 19 mm (3/4 in) thick steel transfer plates (shear key plates) were used to fix the shear keys by fastening ASTM A490 bolts. Note that, as shown in Figure 1, the shear key plates were only placed on one of the sides of the walls, which correspond to the left side of gridline 3 and to the right side of gridline 5, respectively. The steel plates were fastened to the diaphragms using 10 x 140 ASSY VG Plus MTC Solutions screws installed at 45 degrees. Moreover, complete joint penetration (CJP) welds were executed in-situ to transmit the diaphragm forces from the collector plates to the shear transfer plates. Collector plates were Grade 36 steel plates with a cross-section of 6.35 mm x 25.4 mm (0.25 in x 1 in). Besides the collector plates, steel chords were also constructed, as shown in Figure 2, to resist diaphragm bending moments. Steel chords had a cross-section of 6.35 mm x 50.8 mm (0.25 in x 2 in). The collector plates and steel chords were connected to the CLT panels through 6.4 x 90 SDS Simpson Strong-Tie (SDS25312) screws. Additional details of the floor diaphragm and the observed experimental response can be found in Barbosa et al. (2021).

3. ANALYTICAL MODEL FOR DIAPHRAGM DESIGN AND ASSESSMENT

3.1. Force demands

The design strategy adopted for the full-scale two-story mass-timber building structure implied a separation of the lateral force resisting system (LFRS) and the gravity load resisting systems (Pei et al. 2019). Thus, the beams supporting the floors that act as diaphragms are not used as chords to resist diaphragm bending moments. This is accomplished by creating a clear and direct load path for inertial forces to the walls, avoiding the transmission of seismic loading to the gravity system. First principles of mechanics are used along with fastener properties and member strength properties according to the provisions given in related literature and standards (e.g., National Design Specification (NDS) (AWC 2015) and Eurocode 5 (EC5) (CEN 2005)).

As presented in Figure 1, the diaphragm presents a central span, between the walls, and two cantilevers at either end. The diaphragm can be considered as a deep beam, following the recommendations in Wallner-Novak et al. (2014). Let the wind or seismic load effects on the diaphragm be represented by a uniformly distributed load p_d, as shown in Figure 3, which in the case of a seismic load is given by:

$$p_d = D_{LF} \cdot C_{PX} \cdot B \tag{1}$$

where D_{LF} is the seismic weight due to dead loads only and thus does not include a portion of live load, C_{PX} is the seismic design acceleration coefficient, and B is the diaphragm depth. The seismic dead load used was 3.06 kN/m^2, while the live load was neglected. The design of the diaphragm presented in this paper is related to the second phase of the shake-table experiment, described in detail in Blomgren et al. (2019) that considered a site located in Seattle, Washington. The alternative diaphragm design force level method described in Ghosh (2016), which is included in ASCE 7-16 (2017) Section 12.10.3, was used to compute C_{PX}. The mapped short-period spectral response acceleration parameter (S_s) was equal to 1.77 g, which corresponds to a design spectral response acceleration parameter at short periods (S_{DS}) equal to 1.18 g, as defined in Section 11.4.4 of ASCE 7-16 (2017). Using the formulas available in Ghosh (2016), the first mode effect is reduced by an R-factor equal to 4 and amplified by an over-strength Ω_0 equal to 3. The reduction factor, R_s, used to compute the diaphragm design forces was taken equal to 1.0, which results in an acceleration corresponding to an elastic response to a design-level earthquake. The modal contribution modifier, z_S, considered was equal to 1.0 (see Table 2 in Ghosh (2016)), while the importance factor, I_e, was considered equal to 1.0. Thus, the floor level was designed for an earthquake-induced horizontal acceleration that corresponds to a design coefficient C_{PX} equal to 0.83.

The design model presented in Figure 3 neglects the flexibility associated with panel-to-panel and chord splice connections. Consequently, the quantity of screws and their spacing at each surface spline is determined according to the shear flow caused by the inertial forces. The inertial forces are calculated with the seismic mass and the design floor accelerations, which were assumed as uniform, as described above. As presented in Figure 3, the diaphragm studied is only subjected to loading perpendicular to the panel length since this was the direction of loading on the shake-table test. Taking into account the diaphragm configuration, it is assumed that the plywood surface splines SS_1 to SS_9, perpendicular to the loading direction, are subjected to shear forces that arise from in-plane bending. The shear forces can be estimated using the design shear flow model indicated in Figure 3, which is given by the shear flow equation:

$$f_{0,1}\left(x_2, x_3\right) = \frac{v(x_3)}{B}\left[\frac{3}{2} - 6\left(\frac{x_2}{B}\right)^2\right] \tag{2}$$

where $v(x_3)$ is the total transverse shear force in the diaphragm at a coordinate x_3 along the diaphragm length, x_2 is the coordinate along the diaphragm width, and $f_{0,1}\left(x_2, x_3\right)$ is the shear flow of a surface spline oriented perpendicularly to the applied seismic load. Finally, the average design force of a specific fastener is determined by simply multiplying the shear flow by the respective spacing. The plywood surface splines, oriented parallel to N-S direction, are built with Simpson Strong-Tie SDWS22338 spaced at 101.6 mm on center. On the other hand, the plywood surface splines parallel to the loading direction carry in-plane forces from the central part of the diaphragm to the cantilevered part. In this case, each surface spline is designed for a shear flow given by:

$$f_{0,2} = \frac{F_s}{L_s} \tag{3}$$

where F_s is the shear force transmitted through the surface spline, L_s is the respective spline length, and $f_{0,2}$ is the shear flow of a surface spline parallel to the applied seismic load. The plywood surface splines, oriented parallel to E-W direction, are built with Simpson Strong-Tie SDWS22338 spaced at 76.2 mm on center. Table 1 presents the shear flow obtained through Eq. 1 and Eq. 2 for each plywood surface spline while comparing it to the allowable shear flow (strength) provided, which results from the division of the screw strength by the spacing assigned.

The general CLT diaphragm design guidelines outlined in the literature focus on the design of panel-to-panel, chord, and collector connections assuming ductile failure modes (AWC 2021). In addition, the verification of in-plane tension, compression, and shear of CLT panels, as well as shear and normal stresses of plywood surface splines and steel chord splices are performed using capacity-based design principles through the use of overstrength factors. As mentioned above, the glulam beams of this diaphragm are not considered as chord members when determining the in-plane resistance of diaphragms. Chord forces (F_{ch}) on steel straps can be computed through equilibrium and are given by:

$$F_{ch} = \frac{M_s \cdot \alpha}{dS} \tag{4}$$

where M_s is the diaphragm moment induced from design level forces, dS is the distance between the geometric center of the steel plates of two opposite diaphragm chords, and α is an overstrength factor for the chord forces. Note that if the gap on the compression side closes, the compression force would be mainly transferred through the panel-to-panel contact and not the compression plate, and that could lead to variations on the estimated force F_{ch}. Further studies could evaluate the impact of gap closure in chord splice designs. Eq. 4 neglects panel-to-panel compression forces and assumes that steel plates take the compression chord forces as well as the tension chord forces. The chord force is then divided by the number of steel plates assumed for each chord splice. The fasteners used in surface splines and panel-to-beam connections, presented in Figure 1, were not used to meet the requirements for continuity of diaphragm tension chords. Thus, these connections are conservatively neglected. In this example, the overstrength factor α is given by the ratio between the spacing required for the panel-to-panel connection and the spacing provided. Additionally, according to (AWC 2021), chord splices shall be designed with an overstrength factor of 2.0. However, when the lateral loads in screws are controlled by ductile failure modes (Mode IIIs and Mode IV) the overstrength factor can be reduced to 1.5. The number of Simpson Strong-Tie SDS25312 Heavy-Duty Connector screws (n_{screws}) per chord splice is then obtained by dividing the chord force (F_{ch}) by the load carrying capacity (Z') of a laterally loaded screw in a steel-to-timber connection. Note that the group action factor C_g that affects connections built with dowel-type fasteners should be considered in the design. However, in this diaphragm f, the screws used to build the chord splices present a shank diameter equal to 0.242 inches resulting in a C_g equal to 1.0 (AWC 2021). Table 1 presents the forces acting on chords and their respective strength provided through the solutions built for each chord and presented in Figure 2. The overstrength factors of chord splices are higher than 1.5, being equal to 1.65 for chords CS_1 and 2.33 for chords CS_2.

Finally, the collectors consisting of two steel plates fastened to the CLT panels are connected to the shear key plate through complete joint penetration (CJP) welds. Since the shear keys are fastened to the central panels placed at the cantilever spans, one can consider that the corresponding inertial forces are transmitted directly to the walls without passing through the collector plates. The number of screws is determined with a similar method as the one applied in the chord splices capacity estimation, where the average load per collector ($V_{collector}$) is given by:

$$V_{collector} = p_d \cdot \left(\frac{L_c}{2} + L_{cl}\right) \cdot \alpha \tag{5}$$

where p_d is the uniformly distributed load, given by Eq. 1, L_c is the central span of the diaphragm, L_{cl} is the cantilevered span, and α is an overstrength factor for the collector forces.

The applied load and strength values of the connections built within the diaphragm and the fasteners used are presented in Table 1. The strength properties of the diaphragm are obtained following procedures and values of the Load and Resistance Factor Design (LRFD) (Smith and Foliente 2002), including the Format Conversion Factor (K_F), Resistance Factor (ϕ), and Time Effect Factor (λ) per the National Design Specification (AWC 2021) (see NDS tables N1, N2, and N3).

3.2. Diaphragm deflection estimation

The calculation of the diaphragm deflection is essential to conclude whether a diaphragm is considered to be flexible or rigid. According to Moroder et al. (2014), Spickler et al. (2015), and Breneman et al. (2016), the total diaphragm deflection $\Delta_{Diaphragm}$ is associated with the flexural deflection related to chords, shear deformation of the CLT panels, and fastener slip. The diaphragm deflection can be given by the following five-term equation:

$$\Delta_{Diaphragm} = \Delta_{CF} + \Delta_{PS} + \Delta_{SS} + \Delta_{CS} + \Delta_{Col} \tag{6}$$

where Δ_{CF} is the deflection due to chord flexure, Δ_{PS} is the deflection due to the shear deformation of CLT panels, Δ_{SS} is the deflection due to panel-to-panel spline connection slip, Δ_{CS} is the deflection associated with the slip of chord splices, and Δ_{Col} is the deflection associated with the slip of collectors. The examples of deflection calculation of CLT diaphragms available in the literature all refer to simply supported diaphragms. However, the diaphragm considered in this study is characterized by a central part, located between walls, and two cantilever parts. Thus, the deflection equation proposed in this paper is based on the first principles of structural mechanics and aims to be general and applicable to other diaphragm boundary conditions. Considering the model presented in Figure 3, and neglecting tension stresses at panel-to-panel splines, the deflection at a specific point of the diaphragm can be given through the application of the principle of virtual work and given by:

$$\Delta_{Diaphragm} = \sum_{j=1}^{n_{frames}} \int_0^l \left(\frac{M_{0,j}\overline{M_{1,j}}}{(EI)_j} + \frac{V_{0,j}\overline{V_{1,j}}}{G_{eff,j}} \right) dx_3 + \sum_{i=1}^{n_{springs}} \frac{F_{0,i}\overline{F_{1,i}}}{K_{spring,i}} \tag{7}$$

where n_{frames} is the number of frames used to represent the diaphragm, $n_{springs}$ represents the number of springs used to represent distinct connections built in the diaphragm, $M_{0,j}$ is the bending force diagram on frame j, $V_{0,j}$ is the shear force diagram on frame j, and $F_{0,i}$ is the force applied on a specific spring i, which represents a specific connection. The M_0, V_0, and F_0 quantities are calculated based on equilibrium under an external load, as exemplified in the diaphragm scheme presented in Figure 4. On the other hand, the bending force diagram $\overline{M_{1,j}}$ on frame j, the shear force diagram $\overline{V_{1,j}}$ on frame j, and force on a generic spring i $\overline{F_{1,i}}$ are calculated for a unit load $\overline{1}$, which is applied at the position and in direction of the displacement being computed. The supports considered in Figure 4 lead to discontinuities in the internal shear force and bending moment diagrams. Consequently, each span is considered as an independent frame when computing the integrals of Eq. 7, thus n_{frames} represents the number of spans (frames). In Eq. 7, $(EI)_j$ represents the effective bending stiffness, $G_{eff,j}$ represents the effective shear stiffness, and $K_{spring,i}$ is the stiffness of each spring considered. Thus, one can include distinct types of connections in the deflection calculation, as long as the model includes their contribution to the diaphragm load transfer. In order to adapt Eq. 7 to the deflection of a specific diaphragm, one has to consider an equivalent bending stiffness, as well as an equivalent shear stiffness. It is assumed that the effective bending stiffness is associated exclusively with the diaphragm chords, which implies the estimation of a chord width (w_{ch}) and an effective Young's modulus of the chord (E_{ch}). The chord width considered for the CLT diaphragm is equal to 628.7 mm (24.75 in), corresponding to the distance between the inner steel strap and the diaphragm edge, as shown in Figure 3. The width of the chord selected is based on the approach in (Spickler et al. 2015). Recently, Lawson et al. (2023) stated that more research is undoubtedly needed to provide evidence-based values for the effective chord width. The effective Young's modulus is based on the formulae proposed in Flaig and Blaß (2013), which is given by:

$$E_{ch} = \frac{E_{0,L} \cdot t_L + E_{90,T} \cdot t_T}{t_{gross}} \tag{8}$$

where $E_{0,L}$ is the Young's modulus parallel to the grain of the lamellae oriented along the major strength direction, $E_{90,T}$ is the Young's modulus perpendicular to the grain of the lamellae oriented along the minor strength direction, t_L is the total thickness of the lamellae oriented along the major direction, t_T is the total thickness of the lamellae oriented along the minor direction, and t_{gross} is the total thickness of the CLT panel.

The diaphragm under analysis was built with V1 grade 3-ply CLT panels manufactured using No. 2 Douglas fir-Larch lumber in the major strength direction and No. 3 Douglas fir-Larch lumber in the minor strength direction (APA 2018). All the layers have the same thickness of 34.9 mm (1.375 in), while the properties of the two types of lumber are slightly different. In the present study, the parallel to the grain Young's modulus $E_{0,L}$ is equal to 11031.6 MPa (1600 ksi), while the perpendicular to the grain Young's modulus $E_{90,T}$ is equal to 321.8 MPa (46.7 ksi). The effective moment of inertia is given by:

$$I = \frac{A_{ch} \cdot W^2}{2} \tag{9}$$

where A_{ch} is the chord cross-section area given by $w_{ch} \cdot t_{gross}$ (see Figure 3), and W is the distance between the geometric center of the top chord and the geometric center of the bottom chord, which is equal to 5.5 m (18 ft). Thus, the portion of the diaphragm deflection due to chord flexure is given by:

$$\Delta_{CF} = \sum_{j=1}^{n_{frames}} \int_0^l \left(\frac{2 \cdot M_{0,j} \cdot \overline{M_{1,j}}}{E_{ch} \cdot A_{ch} \cdot W^2} \right) dx_3 \tag{10}$$

The effective shear modulus considered herein is based in the proposal made in Bogensperger et al. (2010) for CLT panels without lateral gluing interfaces at the narrow faces, and is given by:

$$G_{eff} = \frac{G_{0,L,mean}}{1 + 6 \cdot \alpha_T \cdot \left(\frac{t_{l,mean}}{w_l} \right)^2} \tag{11}$$

where $G_{0,L,mean}$ is the average shear modulus of the lamellas, $t_{l,mean}$ is the average layer thickness, w_l is the board width, or the mean distance of cracks (or stress reliefs), while α_T is a parameter proposed in Bogensperger et al. (2010) to account for torsion and shear deformation of crossing areas, and is given by:

$$\alpha_T = p \left(\frac{t_{l,mean}}{w_l} \right)^q \tag{12}$$

where q and p are parameters calibrated through Finite Element modeling in Bogensperger et al. (2010) for 3-ply and 5-ply CLT. The values proposed for 3-ply are p = 0.5345 and q = -0.7941. The board width considered herein is equal to 184.2 mm (7.25 in), while the average shear modulus of the lamellas is 824.6 MPa (119.6 ksi). The effective shear area, A^*, considered is equal to the cross-section of the diaphragm ($A^* = B \cdot t_{gross}$). Thus, the portion of the diaphragm displacement due to panel shear deformation is given by:

$$\Delta_{PS} = \sum_{j=1}^{n_{frames}} \int_0^l \left(\frac{V_{0,j}\overline{V_{1,j}}}{G_{eff,j} \cdot B \cdot t_{gross}} \right) dx_3 \tag{13}$$

Several works (Moroder et al. 2014; Spickler et al. 2015; Breneman et al. 2016) have demonstrated that the portion related to connection slip has the greatest impact on the magnitude of the estimated deflection of CLT diaphragms. The present work considers that the diaphragm displacement due to panel-to-panel connection slip is given by:

$$\Delta_{SS} = \sum_{i=1}^{n_{SS,springs}} \frac{F_{0,i}\overline{F_{1,i}}}{K_{SS,i}} = \sum_{i=1}^{n_{SS,springs}} \frac{f_{0,i}\overline{f_{1,i}}}{K_{SS,i}} \cdot a_i^2 \tag{14}$$

where $f_{0,i}$ is the value of shear flow due to external loading, $\overline{f_{1,i}}$ is the value of the shear flow at spring i due to a unit virtual load $\overline{1}$, applied at the location and in the direction of the displacement being measured, a_i is the spacing between fasteners, and $K_{SS,i}$ is the stiffness assumed for surface spline connections. The screws and the different spacing a_i used for surface splines can be consulted in the construction drawings (sections C-C and D-D) provided in Figure 1. The stiffness $K_{SS,i}$ is calculated using the slip modulus equation proposed in AWC (2015) for dowel-type fastener in wood-to-wood connections $\gamma_{ww} = 180,000D^{1.5}$, where D is the shank diameter in inches, and the result is retrieved in pound-force per inch. The work developed in Zahn (1991) concluded that half of the slip modulus is an appropriate value for bearing perpendicular to the grain. Thus, half of the slip modulus is considered herein to account for perpendicular crossing layers as suggested by Spickler et al. (2015). In addition, one has to consider the fact that surface spline stiffness is associated with pairs of screws working in series. Thus, the stiffness of a spring, representing a pair of screws on a surface spline is given by:

$$K_{SS,i} = \frac{\gamma_{ww}}{2 \cdot n_{screws}} \tag{15}$$

where n_{screws} is the number of screws (two), and γ_{ww} is the slip modulus proposed by AWC (2015) for wood-to-wood dowel-type.

The calculation of the displacement portion related to the chord splices contribution is performed herein assuming the mechanical model for the connections as two groups of springs working in series, and therefore each is located at opposite sides of the chord splice connection. When under tension or compression forces, each group of springs can be represented through n_{screws} springs working in parallel. The number of steel plates and the respective fasteners used for the chord splices can be consulted in the construction drawings (sections E-E and plan view A) provided in Figure 2. The slip modulus recommended by AWC (2015) for dowel-type steel-to-wood connections [$\gamma_{sw} = 270,000D^{1.5}$, units of lbs/in, with D as the shank diameter of the screw in inches] is used to calculate the stiffness of each screw while considering the effect of perpendicular layers results on a reduction of 50% per fastener (Zahn 1991). The final stiffness of a chord splice in tension, $K_{CS,tension}$, is given by:

$$K_{CS,tension} = n_{plates} \cdot \left(\frac{1}{\frac{2}{n_{screws} \cdot \gamma_{sw}} + \frac{2}{n_{screws} \cdot \gamma_{sw}}} \right) = \frac{1}{4} \cdot n_{plates} \cdot n_{screws} \cdot \gamma_{sw} \tag{16}$$

where n_{screws} is the number of screws per steel plate in one side of the chord splice, n_{plates} is the number of steel plates per chord, and γ_{sw} is the slip modulus. Assuming that the gap between panels closes under compression forces, one can assume that these forces are resisted by panels under compression and the behavior simulated by two linear elastic springs working in series has a stiffness given by:

$$K_{CS,compression} = \left(\frac{1}{\frac{L_{ch,eff}}{E_{ch} \cdot A_{ch}} + \frac{L_{ch,eff}}{E_{ch} \cdot A_{ch}}} \right) = \frac{E_{ch} \cdot A_{ch}}{2 \cdot L_{ch,eff}} \tag{17}$$

where E_{ch} is the effective Young's modulus, and $L_{ch,eff}$ is the effective length of the compression spring can range from $2 \cdot t_{gross}$ to $6 \cdot t_{gross}$ (Newcombe 2015). Assuming $L_{ch,eff} = 4 \cdot t_{gross}$, the diaphragm displacement due to chord splice deformations is given by:

$$\Delta_{CS} = \sum_{i=1}^{n_{chords}} \frac{F_{0,i}\overline{F_{1,i}}}{K_{CS,i,tension}} + \frac{F_{0,i}\overline{F_{1,i}}}{K_{CS,i,compression}} \tag{18}$$

A similar equation can be used to calculate the portion of the diaphragm displacement related to the slip of the collectors, which is given by:

$$\Delta_{Col} = \sum_{i}^{n_{Col}} \frac{F_{0,i}\overline{F_{1,i}}}{K_{col,i}} \tag{19}$$

where $K_{col,i}$ is the effective stiffness of the collector spring i for a total of n_{Col} springs modeled. In this case, each spring stiffness of these connections is determined assuming screws working in parallel, and is given by:

$$K_{Col} = \frac{1}{2} \cdot n_{screws} \cdot \gamma_{sw} \tag{20}$$

In the scope of this work, the mean stiffness properties were used since the diaphragm under analysis is subjected to a shake-table test. However, it is important to mention that future use of the formulae proposed might require stiffness value adjustments according to the limit state and the standards considered in the design of the building.

4. NUMERICAL MODELING APPROACH FOR CLT DIAPHRAGMS

The numerical modeling approach proposed in this study captures the response of CLT diaphragms under in-plane loads induced by seismic ground shaking. Additionally, the forces transmitted through different types of connections within the diaphragm are obtained, allowing for a reliable design or assessment of mass timber diaphragms. One of the main objectives of the proposed approach is that such an approach must be suitable to be implemented in a general finite element program. The modeling approach is illustrated for two-dimensional analyses but can be extended to three-dimensional models.

The CLT panels are represented through four-node shell elements with orthotropic linear elastic behavior. Their mechanical properties can be obtained by consulting technical information given by suppliers or else by combining that information with formulae given in research papers (Blaß and Fellmoser 2004; Gsell et al. 2007; Brandner et al. 2017). The CLT panels are discretized with a mesh refinement that allows for the assignment of link elements that are connected to adjacent panel nodes, representing the various types of connections included in CLT diaphragms. These link elements represent the shear transfer and the behavior in tension and compression of panel-to-panel connections. The glulam beams that support the panels are represented by linear elastic frame elements with adequate mechanical properties given by manufacturer data. These frame elements are discretized based on the CLT panel mesh size and spacing of fasteners used as part of the CLT-to-beam connections. Moreover, CLT diaphragms include also steel plates (steel straps) that are fastened to act as chord members or collectors, which are discretized as frame elements that are connected to the CLT panel elements using link elements.

A load-controlled pushover analysis is proposed to evaluate the behavior of CLT diaphragms, where nodal loads are applied proportionally to the expected inertial loads. This feature aims to exploit the response of distinct types of connections, where their deformation might change given the load type and direction.

4.1. Application to the case study

A two-dimensional model was built using OpenSeesPy (Zhu et al. 2018), which is a python library of Opensees (McKenna 2011). The discretized mesh used is shown in Figure 4a, where the nodes are equally spaced at 304.8 mm (1 foot). The mechanical properties of all the connections are included in the numerical model through zero-length elements that consider a multi-linear elastic response, where the stiffness can differ pending on the load direction. The Elastic Multi-linear material is available in OpenSeesPy (Zhu et al. 2018) is used since it can model different stiffness in tension and compression. Several nodes share the same coordinates, as indicated in Figure 4b, where a quadrilateral ShellMITC4 element (Dvorkin and Bathe 1984) represents a CLT panel, which is connected to elastic beam-column elements that represent glulam beams.

The elastic links that represent CLT-to-beam connections present a similar stiffness in two orthogonal directions, as illustrated by the force-displacement relationships shown in Figure 4b. As mentioned above, it is necessary to modify the slip modulus to account for the reduction observed for perpendicular to grain forces, as suggested by Zahn (1991). Thus, the stiffness considered for CLT-to-beam connections, $K_{clt,b}$, is given given by:

$$K_{clt,b} = \frac{1}{2} \cdot n_{screws} \cdot \gamma_{ww} \tag{21}$$

where the n_{screws} is the number of screws represented by the link element, and γ_{ww} is the slip modulus of wood-to-wood connections according to AWC (2015).

The steel plates used for collectors and chord straps are represented by elastic beam-column elements and linked to the ShellMITC4 nodes through zero-length elements, as indicated in Figure 4b. Similarly to the CLT-to-beam connections, the stiffness assigned to CLT-to-steel plate links, $K_{clt,sp}$, is equal in both orthogonal directions and is given by:

$$K_{clt,sp} = \frac{1}{2} \cdot n_{screws} \cdot \gamma_{sw} \tag{22}$$

where the n_{screws} is the tributary number of screws represented by the link element, and γ_{sw} is the slip modulus of steel-to-timber connections AWC (2015).

The links used to represent surface splines (Figure 4c) require adequate stiffness values for sliding, tension, and panel closure. The shear stiffness of surface splines is calculated through a simple modification of Eq. 15, thus the shear stiffness of surface spline links is given by:

$$K_{ss,shear} = \frac{1}{2 \cdot n_{screws}} \cdot \gamma_{ww} \cdot n_{pairs} \tag{23}$$

where the number of screws n_{screws} represents the number of screws (two), and n_{pairs} correspond to the number of pairs located in the tributary length of the link (0.5 ft or 1 ft).

The stiffness of a surface spline in tension is calculated assuming the response of two springs working in series, and is given by:

$$K_{ss,tension} = \left(\frac{1}{\frac{2}{n_{screws} \cdot \gamma_{ww}} + \frac{2}{n_{screws} \cdot \gamma_{ww}}} \right) = \frac{1}{4} \cdot n_{screws} \cdot \gamma_{ww} \tag{24}$$

where n_{screws} represents the number of screws per row, corresponding to the number of pairs located in the tributary length of the link per row.

Panel closure is accounted by assigning a compression stiffness to the links that represent surface splines. The value of stiffness varies according to the direction of the surface splines, as presented in Table 2. Figure 4d presents a CLT-to-CLT connection that only works in compression given that panels located at the central part of the diaphragm are not connected through a surface spline. However, it is important to model the compression that arises from gap closure due to its importance in resisting diaphragm moments. Thus, an Elastic Multi-linear material was assigned to zero-length elements with negligible stiffness in tension and a compression stiffness that is equal to the one assigned to the links that represent surface splines. For the case study, since the model is capturing diaphragm displacements relative to the walls, the CLT rocking walls are included as rigid frames by assigning a stiffness value that is 1000 times greater than the value assigned to the beams. In addition, for a comprehensive assessment of the relative displacements between walls and the diaphragm, the degrees of freedom of wall nodes are considered as fully fixed.

Figure 4e illustrates the elements used to simulate the wing connection shown in Figure 2, where rigid frames (with the same properties used for walls) are connected through rigid links to the ShellMITC4 elements to simulate the screws installed at 45 degrees. Note that complete joint penetration (CJP) welds are represented through rigid links. It is considered that the shear key has negligible stiffness in the direction perpendicular to the walls (x), while a rigid link represents the response in the direction parallel to the walls (y). To assess the response of the shear key, one has to assign the rotational stiffness of the shear key ($K_{rot,sk} = 3\, E_s I_{sk}/t_{5ply}$) (Mugabo et al. 2021), which is restrained by the CLT wall panel with a thickness (t_{5ply}) of 6.875 in (174.6 mm), where I_{sk} is the moment of inertia.

The main properties of the numerical model are listed in Table 2. When assessing structures to understand their behavior, expected material properties should be used. Thus, the timber members are independently modeled with their mean properties. According to Bogensperger et al. (2010), the effective shear modulus is dependent on the shear modulus of the boards and on the local torsional moment at the layer interface. A correction factor is considered to account for the number of layers used. The in-plane effective shear modulus ($G_{xy} = G_{eff}$) calculated using Eq. 11 is equal to 575.7 MPa. The longitudinal elastic modulus in the principal directions was computed using the composite theory presented in Blaß and Fellmoser (2004), where the elastic properties of the minor strength direction cross layers were considered. According to the manufacturer technical report (APA 2018), the parallel to the grain Young's modulus $E_{0,L}$ of lamellae oriented with the major strength direction is equal to 11031.6 MPa (1600 ksi), while the respective perpendicular to grain Young's modulus ($E_{0,T} = E_{0,L}/30$) is equal to 367.7 MPa (53.3 ksi). For the lamellae oriented in the minor strength direction the parallel to the grain Young's modulus $E_{90,L}$ is equal to 9652.7 MPa (1400 ksi), while the perpendicular to the grain Young's modulus $E_{90,T}$ is equal to 321.8 MPa (46.7 ksi). An elastic modulus of E_x = 7461.9 MPa and E_y =3462.8 MPa, were obtained for the major (x) and minor directions (y), respectively. Despite the present paper only focusing on the in-plane behavior, the use of ShellMITC4 elements requires values for the Young's modulus perpendicular to grain E_z, and the shear moduli G_{xz} and G_{yz}. The values assigned are based on the ratios available in Gsell et al. (2007), as presented in Table 2. Despite having no influence on the present analysis, the value assigned for E_z is equal to 500 MPa (Lam et al. 2014; Moroder et al. 2014). A longitudinal Young' modulus E_L equal to 12.4 GPa (1800 ksi), and a Poisson coefficient ν equal to 0.3, were assigned to the linear elastic frames representing the glulam beams. A Young's modulus E_s = 200.0 GPa, and a Poisson coefficient ν = 0.26, were assigned to the frames used to model the ASTM A36 steel plates used in chord splices and collectors. It is worth noting that the stiffness of the 45-degree screws used to connect wing plates and CLT panels was not considered in either the analytical models or numerical models. In the future, their inclusion in the modeling could be considered through the use of zero-length elements and the use of the second term of Eq. 7.

5. COMPARISON BETWEEN ANALYTICAL AND NUMERICAL MODELS

An analytical model can be evaluated in terms of effectiveness, which involves a compromise between the time used for the computations and the reliability of the results obtained in terms forces and displacements. Basic principles of structural mechanics were used to derive the equations presented in section 3, with assumptions made so as to produce a conservative capacity estimation.

The great advantage of using detailed numerical models resides in the obtainment of better estimates of force and stress distributions, as well as better predictions of diaphragm deformations, as long as the significant phenomena are modeled. Despite the possibility of considering distinct phenomena such as panel closure and tension forces at surface splines, which were not considered in the analytical model, numerical models will always require more time dedicated to model building, computations, and post-processing. The following sections will present the impact of certain modeling assumptions such as including (or not) the glued laminated timber beams on numerical models, as the analytical model did not consider them. Moreover, different authors (Spickler et al. 2015; Breneman et al. 2016) have shown that slip of surface splines plays an important role in diaphragm deflection values. Thus, the effect of considering different levels of stiffness of the surface splines on the deflection and forces of the diaphragm is also investigated.

Thus, for the sake of comparison between analytical model results and numerical model results, this work includes numerical models without beams (Numerical 1) and numerical models with beams (Numerical 2). In addition, two model variations are considered. In the first, designated as "model A", the stiffness of surface splines is determined based on equations presented in section 3 and section 4, respectively. Second, designated as "model B", the stiffness of surface splines (in shear and tension) derived for model A are multiplied by a factor equal to 5. Even though the factor of 5 is a significant increase and could potentially be perceived as an upper bound of the surface spline stiffness, the value is informed by the ratios between the stiffness of butt joints with inclined screws and plywood surface splines that were obtained experimentally in Loss et al. (2018), as well as by the experimental results obtained in Schiro et al. (2018), which investigated the strength and stiffness of timber-to-timber joints built with inclined screws and timber-to-timber joints made with screws fastened perpendicular to the shear planes.

5.1. Diaphragm deflections

The diaphragm deflections are herein evaluated at two locations of the diaphragm: at the cantilever tip, and at the midspan of the central section of the diaphragm. The largest magnitude of the diaphragm deflection due to the seismic loading and geometry considered in Figure 3 occurs at the cantilever tips. Based on the analytical model shown in Figure 3 and using Eq. 6 to provide a simplified expression for each portion of the diaphragm displacement, analytical expressions are determined based on the loading of various stiffness terms presented in Table 3 where the values obtained for the diaphragm case study are presented. Table 3 also presents the contribution of each portion, evaluated in terms of its percentage of the total displacement obtained. Results indicate that surface spline slip provides the highest contribution for diaphragm deflections.

Figure 5 presents the diaphragm deformations obtained for the numerical models. The numerical model 1A (without beams) reached a maximum displacement of 7.9 mm at the cantilever tip, while the central span deflection is equal to 2.6 mm. For the numerical model 2A (with beams), the maximum deflection is reached at the cantilever tip with a value of 7.1 mm, while the central span reached a deflection of 2.4 mm. Thus, the inclusion of beams reduced the maximum deflection by 11.2%, i.e. by 0.8 mm, which is negligible and supports the decision to neglect them for displacement calculations in the present case.

From the comparison of the displacement diagrams presented in Figure 5a and Figure 5c, it can be concluded that the surface spline stiffness plays a crucial role in the diaphragm deflection. When the stiffness of surface splines is increased 5 times (model 2B), the deflection at the diaphragm tip reduces to 4.5 mm (model 1B), which is 43.4% less than the deflection calculated for model 1A. As mentioned above, the analytical model does not include beams, consequently, its deflection results might be compared with numerical models that do not include beams. Figure 6 summarizes the deflection results obtained for all the models considered in this analysis. In Figure 6b the results of the analytical model were obtained through the consideration of surface splines with a shear stiffness that is 5 times higher than the stiffness presented in Table 3. Results in Figure 6 indicate that the analytical model provides higher deflections than the numerical models. However, the difference is lower for models where the stiffness of surface splines is modeled using the methods and values proposed in the numerical modeling section (model 1A). From results in Figure 6a, the difference between the analytical model and numerical model 1A is 17.8% for the cantilever tip deflection (Δ_{cl}) and 6.8% for the deflection measured in the middle of the diaphragm (Δ_c).

The differences between the deflections obtained through the analytical model and the numerical model 1B are higher, 24.5% for the cantilever tip deflection and 79% for the middle diaphragm deflection. Through the comparison between the values of numerical model 1A and numerical model 2A (Figure 6a), one can observe that the inclusion of beams leads to a reduction of 11% of the maximum deflection of the diaphragm. Thus, this result indicates that even though there is room for an update of the analytical model, by including the deformation of beams and the contribution of CLT-to-beam connections to the floor stiffness, their contribution in this case study was relatively small.

Diaphragm deflections are used to determine whether a diaphragm is considered rigid or flexible. According to ASCE 7-16 (2017), a diaphragm is considered as flexible when its deflection is higher than two times the average story drift. Otherwise, the diaphragm can be considered as rigid and in-plane loads can be considered to be uniformly distributed throughout the area of the diaphragm. From the story drifts measured during the UCSD full-scale two-story shake-table tests, Blomgren et al. (2019) reported that the inter-story drift ratio was under the target of 2.5% (92.5 mm) for all design basis earthquakes (DE). Since the maximum deflection results from the numerical model are 9.4 mm, which is about a tenth of the story drifts measured, or in other words clearly less than two times the average story drift reached during the shake table tests, the diaphragm in this case study would be considered as a rigid diaphragm for the purpose of distributing story shears to the lateral resisting elements.

5.2. Chord forces

As mentioned previously in the paper, the analytical model considers that steel plates used as chord splices are designed to resist all the moments in a specific cross-section of the diaphragm, thus neglecting the contribution of the surface splines to resist moments. However, the numerical models include stiffness in tension and compression for the surface splines located below the chord splices. Therefore, the analytical and numerical models have different internal force distributions in resisting diaphragm moments.

Figure 7 shows a comparison of the tension forces calculated for the chord splices for the different models considered. The analytical model considers that the tension forces are exclusively resisted by the steel straps; the tension force in the central chord splices (CS_1) is equal to 43.9 kN, while the CS_2 steel straps have a tension force of 56.9 kN. The numerical model 1A shows that surface splines carry part of the chord forces, where SS_{12} (see Figure 3) is subjected to smaller tension forces (equal to 21.1 kN) when compared to the force at the same location in the analytical model. The tension forces carried by the steel straps CS_1 and CS_2 reduced by 34% and 46%, respectively. The inclusion of beams in the numerical model 2A further reduces the steel strap forces to 16.7 kN in CS_1, while a reduction of 9% is observed in the forces in CS_2, when compared to the forces in model 1A, i.e., the model in which beams are not explicitly modeled. The maximum tension force carried by the glulam beams is observed at the central span of the diaphragm and is equal to 10.8 kN.

The impact of surface spline stiffness can be evaluated in Figure 7b, where one can conclude that an increase of 500% in the spline stiffness terms resulted in higher tension forces at surface splines SS_{10} and SS_{12}. The surface splines are subjected to 39 kN for both numerical models considered (models 1B and 2B). As expected, Figure 5b confirms that consideration of glulam timber beams influences the forces in chord splices.

5.3. Surface spline forces

The response of surface splines is evaluated in terms of tension force and shear force transfer. Figure 7, discussed in the previous section, shows the impact of surface spline stiffness on the tension forces acting at the surface splines aligned with the walls, where it can be seen that higher stiffness lead to higher tension forces. From the results presented in Figure 8, similar conclusions can be drawn relative to the shear flow values. Figure 8a presents the shear flow obtained for surface splines aligned with the walls for model 1A, i.e. considering the stiffness provided through Eq. 23 and not including beams in the numerical model. The influence on the shear flow of surface splines, when beams are added to the structural model, can be observed in Figure 8b, whereby an increase of 3.5% on the shear flow of the tension chord surface splines is observed. On the other hand, the shear flow reduces by 6% for the surface splines positioned at the compression chords.

Figure 9 presents the shear flow for surface splines aligned with walls for models 1B and 2B, or in other words when splices are modeled with increased stiffness. Through the inclusion of beams in the modeling, the shear flow is reduced (4.6%) at the compression side and increased (1.2%) at the tension side.

The shear flow obtained through the analytical model is based on the total transverse shear force, as per Eq. 2. Figure 10 allows to compare the shear flow calculated through Eq. 2 and the shear flow obtained through the numerical models. From the numerical models results presented in Figure 10, one can conclude that some of the assumptions behind the simple analytical beam model are not accurate for internal stresses. The rigid nature of the panels relative to the connections can lead to a redistribution of shear stress towards the average stress along the length of the surface spline connection, as shown in see results for models 1A and 2A in Figure 10a and 10b, respectively. On the other hand, when the stiffness of connections increases 5 times the shear flow obtained through the numerical model reaches higher values near the walls and an almost linear reduction towards the tip of the diaphragm, as shown in see results for models 1B and 2B in Figure 10c and 10d, respectively. These results reinforce that the relative stiffness between panels and connections influences the stress distribution. The analytical model proposed provides better estimates for panel-to-panel connections modeled with stiffer elements. As the stiffness of the panel-to-panel connections is reduced, the numerical model tends to even out the shear stresses along the spline length, indicating that it may be reasonable to consider a uniform stress distribution when designing these elements.

Figure 11 shows the tension forces distributed along the longitudinal axis of surface spline SS_3. It is possible to conclude that this spline is subjected to tension forces near the fixed end, indicating that these forces should be considered in the spline design as not including them in the design could lead to unconservative results. In addition, the numerical models that included 5 times higher stiffness in the modeling of the surface splines (model 1B and 2B) develop tension forces that are close to twice the values obtained from the numerical models with the original stiffness (model 1A and 2A), reinforcing the importance of adequate consideration of the stiffness of the splines as well as their tension force demands in design, which are currently neglected.

5.4. Collector forces

Figure 12 shows the shear flow acting on the screws along the collector, which varies along its length, in contrast with the uniform shear flow assumption used in the design and in the development of the analytical model. Numerical model 2A considers beams and allows to conclude that they have an impact on the shear flow acting on the collector screws that are fastened in the region located near the compression chords. Indeed, the tension forces are directly related to the relative displacement between adjacent CLT panels. Thus, the inclusion of surface splines with higher tension stiffness led to smaller relative displacements, which in turn reduces the force demands on the collectors, as can be seen in the results presented in Figure 12c and Figure 12d. For reference, the maximum collector tension force for the numerical model 2A is equal to 17.3 kN, while for numerical model 2B it is equal to 12.7 kN, which results in a reduction of 26.6%.

5.5. Discussion

One of the main findings from results discussed in this section is related to the impact that the surface spline stiffness has on the shear flow, which can be observed from results in Figures 8, 9, and 10. Results indicate that the force distributions within a numerical model of a diaphragm greatly depend on the stiffness of elements and connections. Therefore, it is crucial that realistic, expected stiffness values are used in the modeling and that these are supported by experimental tests. In addition, the analytical models provided reasonable force distributions when compared to the numerical models, although the forces obtained from the analytical models were not always conservative, especially when beams were also considered in the numerical models. Note that further research should be performed to verify the appropriate slip modulus of the distinct connections used in the diaphragm. For example, the adequacy of a weighted slip modulus considers the depth of the fastener into the individual laminae, as the bearing is split between the parallel and perpendicular laminae. The formulae presented in Eq. 15, Eq. 16, and Eq 20 are based on the assumed reduction of 50%, as recommended in Spickler et al. (2015). A different percentage of reduction leads to different equations for the calculation of K_{SS}, $K_{CS,tension}$, and K_{Col}.

While the proposed models are founded on sound fundamental principles, it's recognized that further calibration against empirical data will enhance their accuracy and reliability. This research primarily aimed to establish a framework for various mass timber diaphragms, acknowledging the inherent limitations of such an approach without extensive experimental validation. Future efforts will focus on refining these models to enhance their robustness and practicality by incorporating additional experimental data results. Given the inherent calibration in finite element modeling, it's understood that this approach can greatly improve the accuracy of a single model in isolation. Taylor et al. (2020) provided crucial results for surface splines characterization; however, additional tests are still paramount, especially ones related to the chord splices utilized in diaphragms. Therefore, mitigating the extensive calibration of FEMs needed and improving model accuracy, remains a priority for future research.

6. CONCLUSION

This study presents both analytical and numerical models, which aid in the design and assessment of mass timber diaphragms to wind and seismic lateral loads. The analytical model is based on basic principles of mechanics and requires fastener properties and member strength and stiffness properties, which can be obtained from information available in the literature or in codes, such as NDS. The use of the analytical model in design, in particular for the case study diaphragm, allows for sufficient redundancy which is a crucial condition of the experimental campaign in Barbosa et al. (2021) since the diaphragm was subjected to 34 earthquakes with little to no damage. The analytical model proposed led to conservative results both in terms of deflections and forces when compared to the numerical models that included identical phenomena and sources of stiffness and strength. However, the inclusion of beams in the numerical model, which are not considered in the analytical model, identified some under predictions of the forces obtained using the analytical model compared to those obtained in the numerical modeling results. Nonetheless, from the observed differences between analytical and numerical results, the overall force distributions obtained from the analytical model are useful for design.

A numerical modeling approach for mass timber diaphragms was presented. The numerical model aims to simulate the response of mass timber diaphragms by considering the most salient features. The forces transmitted through different types of connections within the diaphragm can be captured through the use of zero-length elements (links), allowing improved estimates of deformations and internal forces for use in refined design or assessment of CLT diaphragms.

An analytical model was presented to estimate diaphragm deflections under lateral loading, which accounts for five phenomena including chord flexure, panel shear, panel-to-panel shear connection slip, chord splice slip, and collector slip. Based on comparisons of the results obtained from the analytical model with the numerical model results, the phenomena included in the model were sufficient to capture the responses and led to similarly predicted displacements. However, the five-term analytical model can be further improved by considering additional phenomena, such as panel-to-beam connections, beams in tension, and surface splines in tension. While the deflection analytical model is practical and useful for design since it does slightly over-predict diaphragm deformations, the numerical modeling approach can produce improved estimates of forces and deformations in those cases where the analytical model is not appropriate for quantification of diaphragm deflections. In addition, the numerical models can be used in the future to conduct various sensitivity studies to assess the impact of various engineering parameters, such as the slip modulus of connections and the importance of friction for screwed connections, among others.

Based on the findings reported in this paper, one can state that the analytical model presented is suitable for the design of symmetric diaphragms with regular shapes. However, since this paper only considers one case study, additional shapes and boundary conditions should be assessed prior to applying the methods generally.

7. DATA AVAILABILITY STATEMENT

Some or all data, models, or code that support the findings of this study are available from the corresponding author upon reasonable request.

8. ACKNOWLEDGMENTS

The first author would like to acknowledge the support of the Portuguese Science Foundation (FCT), through PhD grant PD/BD/113679/2015 included in InfraRisk-PhD program. The first author would also like to acknowledge the support of Oregon State University during the period in which he was a visiting Ph.D. student at this institution. The first, second, and tenth author were partially financed by FEDER funds through the Competitivity and Internationalization Operational Programme COMPETE, Portugal 2020, and by FCT – Portuguese Foundation for Science and Technology - funds within the scope of the Timquake project POCI-01-0145-FEDER-032031.

This work was financially supported by USDA Agricultural Research Service in cooperation with the Tallwood Design Institute under the grant number $58-0204-6-002$. Additional thanks to Simpson Strong-Tie and DR Johnson for their support. This research project was also supported by the US National Science Foundation through a number of collaborative awards, including CMMI 1636164, CMMI 1634204, and CMMI 1634628. The use of the referenced shake table experimental facility is supported by the National Science Foundation's Natural Hazards Engineering Research Infrastructure (NHERI) Program. The authors would like to especially thank the NHERI at University of California San Diego site management and staff, who helped greatly in the construction and testing program. The authors also would like to acknowledge individual industry collaborators and students who worked on this project, including Brian DeMeza, Jace Furley, Gabriele Tamagnone, Daniel Griesenauer, Ethan Judy, Steven Kordziel, Aleesha Busch, Ali Hansan, Joycelyn Ng, Monica Y. Liu, and Ata Mohseni. The opinions presented are solely those of the authors and do not reflect opinions or endorsements of the funding agencies.

REFERENCES

APA (2008). *Glulam Product Guide*. Tacoma, Washington, USA.

APA (2017). *ANSI/APA PRG-320 - Standard for Performance-Rated Cross-Laminated Timber*. Tacoma, Washington, USA.

APA (2018). *APA PR-L320 DRJ Cross-Laminated Timber*. Tacoma, Washington, USA.

ASCE 7-16 (2017). *Minimum Design Loads and Associated Criteria for Buildings and Other Structures (7-16)*. American Society of Civil Engineers.

AWC (2015). *National Design Specification for Wood Construction*. Leesburg, Virginia.

AWC (2021). *National Design Specification for Wood Construction*. Leesburg, Virginia.

Barbosa, A. R., Rodrigues, L. G., Sinha, A., Higgins, C., Zimmerman, R. B., Breneman, S., Pei, S., van de Lindt, J. W., Berman, J., and McDonnell, E. (2021). "Shake-table experimental testing and performance of topped and untopped cross-laminated timber diaphragms." *Journal of Structural Engineering*, 147(4), 04021011.

Beairsto, C., Gupta, R., and Miller, T. H. (2022). "Monotonic and cyclic behavior of clt diaphragms." *Practice Periodical on Structural Design and Construction*, 27(2), 04021085.

Blaß, H. and Fellmoser, P. (2004). "Design of solid wood panels with cross layers." *8th WCTE World Conference on Timber Engineering*, Lahti, Finland.

Blomgren, H., Pei, S., Jin, Z., Powers, J., Dolan, J., van de Lindt, J., Barbosa, A., and Huang, D. (2019). "Full-Scale Shake Table Testing of Cross-Laminated Timber Rocking Shear Walls with Replaceable Components." *Journal of Structural Engineering*, 145(10), 04019115.

Bogensperger, T., Moosbrugger, T., and Silly, G. (2010). "Verification of CLT-Plates under loads in plane." *11th WCTE World Conference on Timber Engineering 2010*.

Branco, J. M., Kekeliak, M., and Lourenço, P. B. (2015). "In-plane stiffness of timber floors strengthened with clt." *European Journal of Wood and Wood Products*, 73(3), 313–323.

Brandner, R., Dietsch, P., Dröscher, J., Schulte-Wrede, M., Kreuzinger, H., and Sieder, M. (2017). "Cross Laminated Timber (CLT) Diaphragms Under Shear: Test configuration, Properties and Design." *Construction and Building Materials*, 147, 312–327.

Breneman, S., McDonnell, E., and Zimmerman, R. (2016). "An approach to CLT Diaphragm Modeling for Seismic Design with Application to a U.S. High-Rise Project." *14th WCTE World Conference on Timber Engineering*, Vienna, Austria.

Ceccotti, A., Lauriola, M., Pinna, M., and Sandhaas, C. (2006). "SOFIE project–cyclic tests on cross-laminated wooden panels." *9th WCTE World Conference on Timber Engineering*, Portland, Oregon, USA.

Ceccotti, A., Sandhaas, C., Okabe, M., Yasumura, M., Minowa, C., and Kawai, N. (2013). "SOFIE project – 3D shaking table test on a seven-storey full-scale cross-laminated timber building." *Earthquake Engineering & Structural Dynamics*, 42(13), 2003–2021.

CEN (2005). *EN 1995-1-1:2005, Design of timber structures. P. 1-1: General - Common rules and rules for buildings*. European Committee for Standardisation.

Dröscher, J. (2014). "Prüftechnische Ermittlung der Schubkenngrößen von BSPScheibenelementen und Studie ausgewählter Parameter (in German)." M.S. thesis, Graz University of Technology, Graz, Austria.

Dujic, B., Strus, K., Zarnic, R., and Ceccotti, A. (2010). "Prediction of Dynamic Response of a 7-Storey Massive XLam Wooden Building Tested on a Shaking Table." *11th WCTE World Conference on Timber Engineering*, Riva del Garda, Italy.

Dvorkin, E. N. and Bathe, K.-J. (1984). "A continuum mechanics based four-node shell element for general non-linear analysis." *Engineering computations*.

D'Arenzo, G., Casagrande, D., Reynolds, T., and Fossetti, M. (2019). "In-plane elastic flexibility of cross laminated timber floor diaphragms." *Construction and Building Materials*, 209, 709–724.

Flaig, M. and Blaß, H. (2013). "Shear strength and shear stiffness of CLT-beams loaded in plane." *In: Proceedings. CIB-W18 Meeting 46*.

Ganey, R., Berman, J., Akbas, T., Loftus, S., Dolan, J. D., Sause, R., Ricles, J., Pei, S., van de Lindt, J. W., and Blomgren, H.-E. (2017). "Experimental Investigation of Self-Centering Cross-Laminated Timber Walls." *Journal of Structural Engineering*, 143(10), 04017135.

Ghosh, S. (2016). "Alternative Diaphragm Seismic Design Force Level of ASCE 7-16." *Structure*

Magazine.

Gsell, D., Feltrin, G., Schubert, S., Steiger, R., and Motavalli, M. (2007). "Cross-Laminated Timber Plates: Evaluation and Verification of Homogenized Elastic Properties." *Journal of Structural Engineering*, 133(1), 132–138.

Harris, R., Ringhofer, A., and Schickhofer, G. (2013). *Focus Solid Timber Solutions - European Conference on Cross Laminated Timber (CLT)*. University of Bath.

Harte, A. M. (2017). "Mass timber – the emergence of a modern construction material." *Journal of Structural Integrity and Maintenance*, 2(3), 121–132.

Hossain, A., Lakshman, R., and Tannert, T. (2016). "Shear Connections with Self-tapping-screws for Cross-laminated Timber Panels." *WCTE (World Conference on Timber Engineering)*, Vienna, Austria.

Hossain, A., Lakshman, R., and Tannert, T. (2017). "Cyclic Performance of Shear Connections with Self-tapping-screws for Cross-laminated Timber Panels." *WCEE (World Conference on Earthquake Engineering)*, Santiago, Chile.

Hossain, A., Popovski, M., and Tannert, T. (2019). "Group Effects for Shear Connections with Self-Tapping Screws in CLT." *Journal of Structural Engineering*, 148(8), 1–9.

Iqbal, A., Pampanin, S., Palermo, A., and Buchanan, A. H. (2015). "Performance and Design of LVL Walls Coupled with UFP Dissipaters." *Journal of Earthquake Engineering*, 19(3), 383–409.

Kode, A., Amini, M. O., van de Lindt, J. W., and Line, P. (2021). "Lateral load testing of a full-scale cross-laminated timber diaphragm." *Practice periodical on structural design and construction*, 26(2), 04021001.

Kohler, J., Fink, G., and Brandner, P. (2016). "Basis of design principles – application to CLT." *Cross Laminated Timber – a competitive wood product for visionary and fire safe buildings: Joint Conference of COST Actions FP1402 and FP1404*, Stockholm, Sweden.

Lam, F., Haukaas, T., and Ashtari, S. (2014). "In-plane stiffness of cross-laminated timber floors." *World Conference on Timber Engineering*, 1–10.

Lawson, J., Breneman, S., and Ricco, M. L. (2023). "Wood diaphragm deflections. ii: Implementing a unified approach for current clt and wsp practice." *Journal of Architectural Engineering*, 29(3), 04023020.

Li, H., Wang, B. J., Wei, P., and Wang, L. (2019). "Cross-laminated Timber (CLT) in China: A State-of-the-Art." *Journal of Bioresources and Bioproducts*, 4(1), 22–30.

Loss, C., Hossain, A., and Tannert, T. (2018). "Simple cross-laminated timber shear connections with spatially arranged screws." *Engineering Structures*, 173, 340–356.

McKenna, F. (2011). "Opensees: a framework for earthquake engineering simulation." *Computing in Science & Engineering*, 13(4), 58–66.

Moroder, D., Smith, T., Pampanin, S., Palermo, A., and Buchanan, A. H. (2014). "Design of floor diaphragms in multi-storey timber buildings." *International Network on Timber Engineering Research. Bath, United Kingdom*.

Mugabo, I., Barbosa, A. R., Sinha, A., Higgins, C., Riggio, M., Pei, S., van de Lindt, J. W., and Berman, J. W. (2021). "System identification of ucsd-nheri shake-table test of two-story structure with cross-laminated timber rocking walls." *Journal of Structural Engineering*, 147(4).

Nairn, J. A. (2019). "Predicting layer cracks in cross-laminated timber with evaluations of strategies for suppressing them." *European Journal of Wood and Wood Products*, 77(3), 405–419.

Newcombe, M. P. (2015). "The connection response of rocking timber walls." *NZ SESOC Journal*, 28(1), 46–53.

Passarelli, R. and Koshihara, M. (2018). "The Implementation of Japanese CLT: Current Situation and Future Tasks." *15th WCTE World Conference on Timber Engineering*, Seoul, Rep. of Korea.

Pei, S., van de Lindt, J., Barbosa, A., Berman, J., McDonnell, E., Dolan, J., Blomgren, H., Zimmerman, R., Huang, D., and Wichman, S. (2019). "Experimental Seismic Response of a Resilient 2-Story Mass-Timber Building with Post-Tensioned Rocking Walls." *Journal of Structural Engineering*, 145(11), 04019120.

Pei, S., van de Lindt, J. W., Popovski, M., Berman, J. W., Dolan, J. D., Ricles, J., Sause, R., Blomgren, H., and Rammer, D. R. (2016). "Cross-Laminated Timber for Seismic Regions: Progress and Challenges for Research and Implementation." *Journal of Structural Engineering*, 142(4), 1–11.

Popovski, M., Schneider, J., and Schweinsteiger, M. (2010). “Lateral load resistance of cross-laminated wood panels.” *11th WCTE World Conference on Timber Engineering*, 4, 3394–3403.

Schiro, G., Giongo, I., Sebastian, W., Riccadonna, D., and Piazza, M. (2018). “Testing of timber-to-timber screw-connections in hybrid configurations.” *Construction and Building Materials*, 171, 170–186.

Smith, I. and Foliente, G. (2002). “Load and resistance factor design of timber joints: International practice and future direction.” *Journal of structural engineering*, 128(1), 48–59.

Spickler, K., Closen, M., Line, P., and Pohll, M. (2015). “Cross laminated timber horizontal diaphragm design example.” *Report no.*, CLT White paper. https://mtcsolutions.com/wp-content/uploads/2019/04/CLT_Horizontal_Diaphragm_Design_Example.pdf.

Standards New Zealand (1993). *NZS 3603 Timber Structures Standard*. Wellington,Washington, New Zealand.

Sullivan, K., Miller, T. H., and Gupta, R. (2018). “Behavior of Cross-Laminated Timber Diaphragm Panel-to-Panel Connections with Self-Tapping Screws.” *Engineering Structures*, 168, 505–524.

Sustersic, I., Fragiacomo, M., and Dujic, B. (2016). “Seismic Analysis of Cross-Laminated Multistory Timber Buildings Using Code-Prescribed Methods: Influence of Panel Size, Connection Ductility, and Schematization.” *Journal of Structural Engineering*, 142(4), E4015012.

Taylor, B., Barbosa, A. R., and Sinha, A. (2020). “Cyclic performance of in-plane shear cross-laminated timber panel-to-panel surface spline connections.” *Engineering Structures*, 218, 110726.

Thiel, A. and Brandner, R. (2016). “Design of CLT Elements–Basics and some Special Topics.” *Cross laminated Timber – a competitive wood product for visionary and fire safe buildings: Joint Conference of COST Actions FP1402 and FP1404*, Stockholm, Sweden.

van de Lindt, J. W., Bahmani, P., Mochizuki, G., Pryor, S. E., Gershfeld, M., Tian, J., Symans, M. D., and Rammer, D. (2016). “Experimental Seismic Behavior of a Full-Scale Four-Story Soft-

Story Wood-Frame Building with Retrofits. II: Shake Table Test Results." *Journal of Structural Engineering*, 142(4), E4014004.

van de Lindt, J. W., Furley, J., Amini, M. O., Pei, S., Tamagnone, G., Barbosa, A. R., Rammer, D., Line, P., Fragiacomo, M., and Popovski, M. (2019). "Experimental seismic behavior of a two-story clt platform building." *Engineering Structures*, 183, 408–422.

van de Lindt, J. W., Pei, S., Pryor, S. E., Shimizu, H., and Isoda, H. (2010). "Experimental Seismic Response of a Full-Scale Six-Story Light-Frame Wood Building." *Journal of Structural Engineering*, 136(10), 1262–1272.

Wallner-Novak, M., Koppelhuber, J., and Pock, K. (2014). "Cross-laminated timber structural design—basic design and engineering principles according to eurocode." *proHolz, Østerike*.

Zahn, J. J. (1991). "Design equation for multiple-fastener wood connections." *Journal of structural engineering*, 117(11), 3477–3486.

Zhu, M., McKenna, F., and Scott, M. H. (2018). "Openseespy: Python library for the opensees finite element framework." *SoftwareX*, 7, 6–11.

List of Tables

TABLE 1. Applied forces and respective strength provided for distinct connections of the diaphragm

Connection	Parameter	Applied Value	Strength provided	Screw strength (Z')
$SS_{1,3,7,9}$[a]	shear flow	17.4 N/mm	24.1 N/mm	2447.9 N
$SS_{2,8}$[a]	shear flow	23.3 N/mm	24.1 N/mm	2447.9 N
$SS_{4,6}$[a]	shear flow	7.8 N/mm	24.1 N/mm	2447.9 N
SS_5[a]	shear flow	10.5 N/mm	24.1 N/mm	2447.9 N
SS_{10-13}[b]	shear flow	18.9 N/mm	32.1 N/mm	2447.9 N
Col[c]	shear force	106.1 kN	125.0 kN	4031.9 N
CS_1[e]	chord force	43.9 kN	72.6 kN	4031.9 N
CS_2[d]	chord force	56.9 kN	133.1 kN	4031.9 N

[a] Simpson Strong - Tie 5.6 x 86 TRUSS/EWP PLY screws at 101.6 mm (4 in) on-center
[b] Simpson Strong - Tie 5.6 x 86 TRUSS/EWP PLY screws at 76.2 mm (3 in) on-center
[c] Simpson Strong - Tie 6.4 x 90 (SDS25312) - a total of 36 screws
[d] Simpson Strong - Tie 6.4 x 90 (SDS25312) - a total of 18 screws per CLT panel
[e] Simpson Strong - Tie 6.4 x 90 (SDS25312) - a total of 33 screws per CLT panel
1 N/mm = 68.52 lb/ft
1 kN = 0.225 Kips

TABLE 2. Parameters of the numerical model

Element	Property	Equation	Value	Units
CLT panels	E_x	$\frac{E_{0,L} \cdot t_L + E_{90,T} \cdot t_T}{t_{gross}}$	7461.9	MPa
	E_y	$\frac{E_{90,L} \cdot t_L + E_{0,T} \cdot t_T}{t_{gross}}$	3462.8	MPa
	E_z	-	500	MPa
	G_{xy}	$\frac{G_{0,L,mean}}{1+6 \cdot \alpha_T \cdot \left(\frac{t_{l,mean}}{w_l}\right)^2}$	575.7	MPa
	G_{xz} [a]	$0.065E_L$	483.6	MPa
	G_{yz} [a]	$0.011E_L$	85.0	MPa
Surface splines (N-S)	$K_{ss,shear}$	(23)	2424.0	N/mm
	$K_{ss,tension}$	(24)	1212.0	N/mm
	$K_{ss,compression}$	$\frac{E_y \cdot A_{y,eff}}{2 \cdot L_{y,eff}}$	131837.9	N/mm
Surface splines (E-W)	$K_{ss,shear}$	(23)	3232.0	N/mm
	$K_{ss,tension}$	(24)	1616.0	N/mm
	$K_{ss,compression}$	$\frac{E_x \cdot A_{x,eff}}{2 \cdot L_{x,eff}}$	284093.0	N/mm
Chord splice 1	$K_{clt,sp,1}$	(22)	25341.1	N/mm
Chord splice 2	$K_{clt,sp,2}$	(22)	15486.2	N/mm
Collector	$K_{clt,col}$	(22)	6757.6	N/mm
CLT to beams	$K_{clt,b}$	(21)	1616.0	N/mm
CLT to CLT	$K_{clt-to-clt,x}$	$\frac{E_x \cdot A_{x,eff}}{2 \cdot L_{x,eff}}$	284093.0	N/mm
	$K_{clt-to-clt,y}$	$\frac{E_y \cdot A_{y,eff}}{2 \cdot L_{y,eff}}$	131837.8	N/mm
Wall to shear key	$K_{rot,sk}$	$\frac{3E_s I_{sk}}{t_{5ply}}$	2678972.1	N.m/rad

1 MPa = 0.145 ksi
[a] retrieved from Gsell et al. (2007)

TABLE 3. Displacement values obtained for the diaphragm through the analytical model

Displacement at cantilever tip		
Mode	Equation	Displacement
Chord flexure	$\Delta_{CF,cl} = \left(\frac{L_{cl}^4}{4} + \frac{L_{cl}^3 L_c}{2} - \frac{L_{cl} L_c^3}{12}\right) \frac{p_d}{E_{ch} \cdot A_{ch} \cdot W^2}$	0.93 mm (0.037 in, 10%)
Panel shear	$\Delta_{PS,cl} = \frac{p_d \cdot L_{cl}^2}{2 \cdot G_{eff} \cdot t_{gross} \cdot B}$	0.78 mm (0.031 in, 8.4%)
Surface splines	$\Delta_{SS,cl} = \frac{306 \cdot a^3 \cdot p_d}{64 \cdot B^2 \cdot K_{SS,1-9}} \sum_{i=1}^{n_{pairs}} i$	4.74 mm (0.187 in, 50.4%)
Collectors	$\Delta_{Col,cl} = \frac{p_d \cdot L_{cl}}{2 \cdot K_{Col}}$	0.49 mm (0.019 in, 5.2%)
Chord Splice 1	$\Delta_{CS_1,cl} = \left(\frac{p_d \cdot L_{cl}^3}{2 \cdot dS_2^2} - \frac{p_d \cdot L_c^2 L_{cl}}{8 \cdot dS_2^2}\right) \cdot \left(\frac{1}{K_{\text{CS,1,tension}}} + \frac{1}{K_{\text{CS,compression}}}\right)$	0.98 mm (0.039 in, 10.4%)
Chord Splice 2	$\Delta_{CS_2,cl} = \frac{p_d \cdot L_{cl}^3}{2 \cdot dS_1^2} \cdot \left(\frac{1}{K_{\text{CS,2,tension}}} + \frac{1}{K_{\text{CS,compression}}}\right)$	1.43 mm (0.056 in, 15.2%)
	$\Delta_{Total,cl} =$	9.4 mm (0.37 in)
Displacement at the centre		
Chord flexure	$\Delta_{CF,c} = \left(\frac{5 p_d L_c^4}{192} - \frac{p_d L_{cl}^2 L_c^2}{8}\right) \frac{1}{E_{ch} \cdot A_{ch} \cdot W^2}$	-0.12 mm (-0.005 in, -4.3%)
Panel shear	$\Delta_{PS,c} = \frac{p_d \cdot L_c^2}{8 \cdot G_{eff} \cdot t_{gross} \cdot B}$	0.16 mm (0.006 in, 5.8%)
Surface splines [(a)]	$\Delta_{SS,c} = \frac{p_d \cdot L_c}{2 \cdot K_{SS,10-13}} + \frac{153 \cdot a^3 \cdot p_d}{64 \cdot B^2 \cdot K_{SS,1-9}} \sum_{i=1}^{n_{pairs}} i$	2.74 mm (0.108 in, 98.9%)
Collector	$\Delta_{Col,c} = \frac{p_d \cdot L_c}{2 \cdot K_{Col}}$	0.44 mm (0.0175 in, 15.9%)
Chord splice 1	$\Delta_{CS,c} = \left(\frac{p_d \cdot L_c^3}{32} - \frac{p_d \cdot L_c L_{cl}^2}{8}\right) \cdot \frac{1}{dS_1^2} \cdot \left(\frac{1}{K_{\text{CS,1,tension}}} + \frac{1}{K_{\text{CS,compression}}}\right)$	-0.44 mm (-0.0174 in, -15.9%)
	$\Delta_{Total,c} =$	2.77 mm (0.109 in)
Stiffness variables		
E_{ch} = 7461.7 MPa (1082.2 ksi)		Eq. 8
G_{eff} = 575.7 MPa (83.5 ksi)		Eq. 11
$K_{SS,1-9}$ = 808 N/mm (4614 lb/in)		Eq. 15
$K_{SS,10-13}$ = 24239.6 N/mm (138418.2 lb/in)		Eq. 15
$K_{\text{CS,1,tension}}$ = 25341.1 N/mm (144708 lb/in)		Eq. 16
$K_{\text{CS,2,tension}}$ = 46458.7 N/mm (265298.5 lb/in)		Eq. 16
$K_{\text{CS,compression}}$ = 585970 N/mm (3345972.8 lb/in)		Eq. 17
K_{Col} = 95733.1 N/mm (546675.9 lb/in)		Eq. 20

[(a)] a = 101.6 mm (4 in), screw spacing at SS_1 to SS_9, see Figure 3

List of Figures

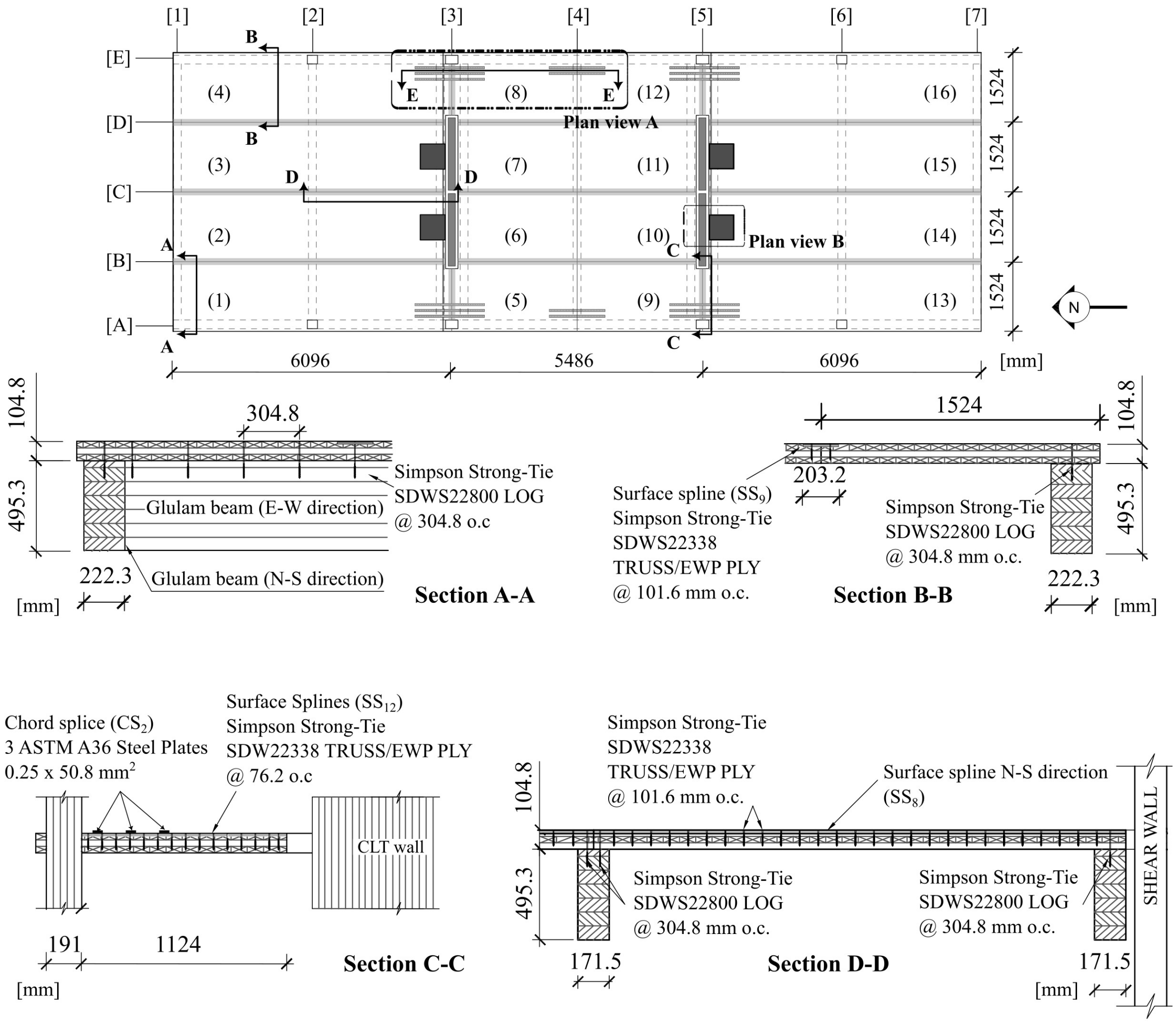

Fig. 1. Diaphragm plan view and details related to plywood surface splines and panel connection at diaphragm boundary.

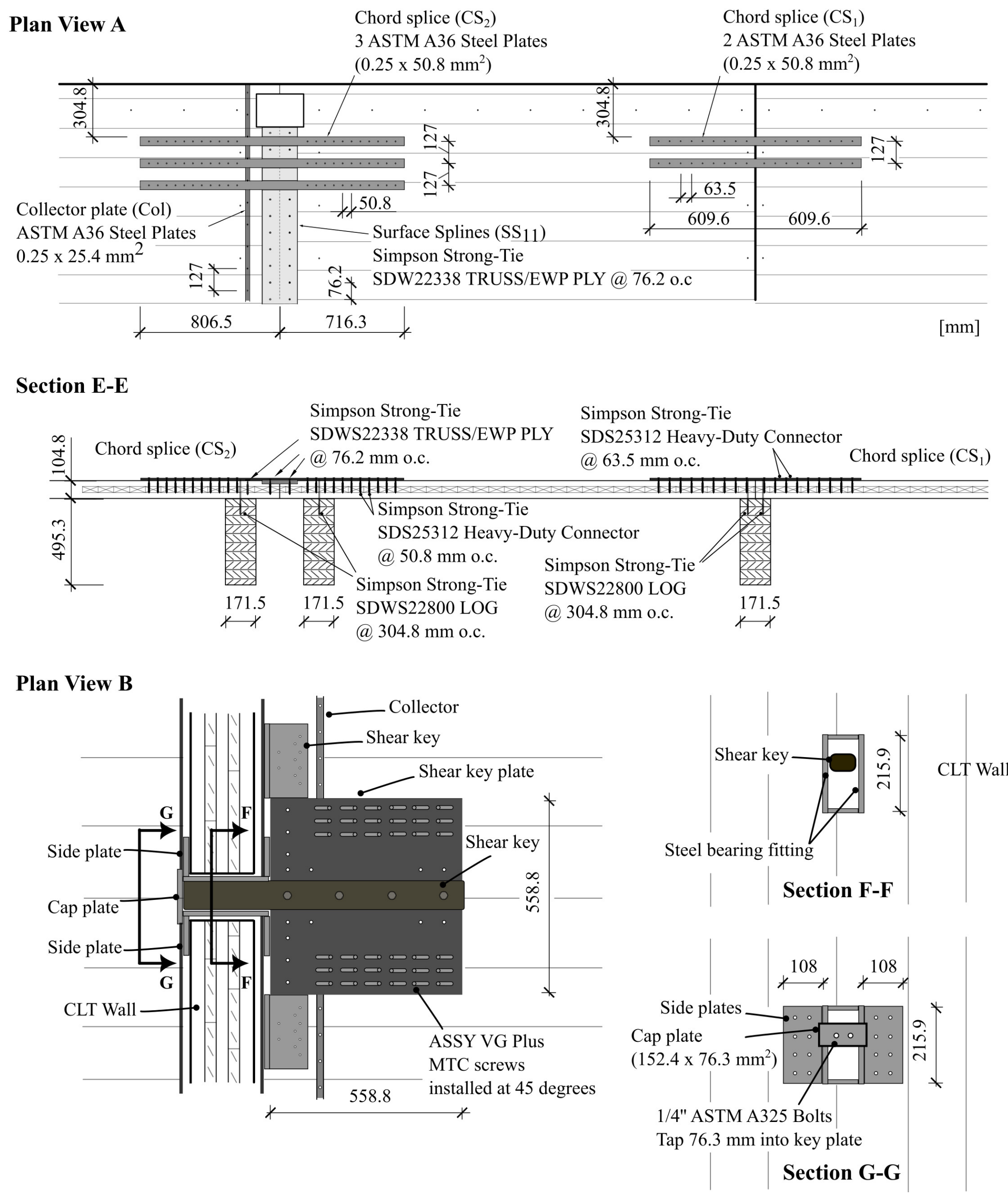

Fig. 2. Diaphragm details with sections related to chord splices and shear key connection

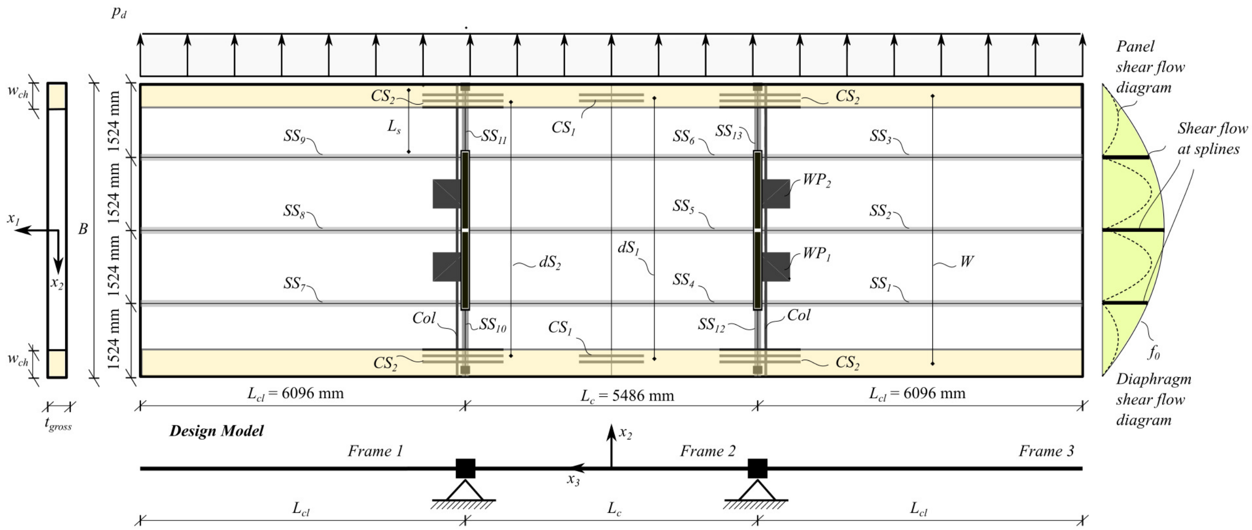

Fig. 3. Diaphragm elements and model assumptions used in the diaphragm design (25.4 mm is equal to 1.0 in). SS_i represent surface splines; CS_i represent chord splices; Col represent collectors. Other variables are described in the text.

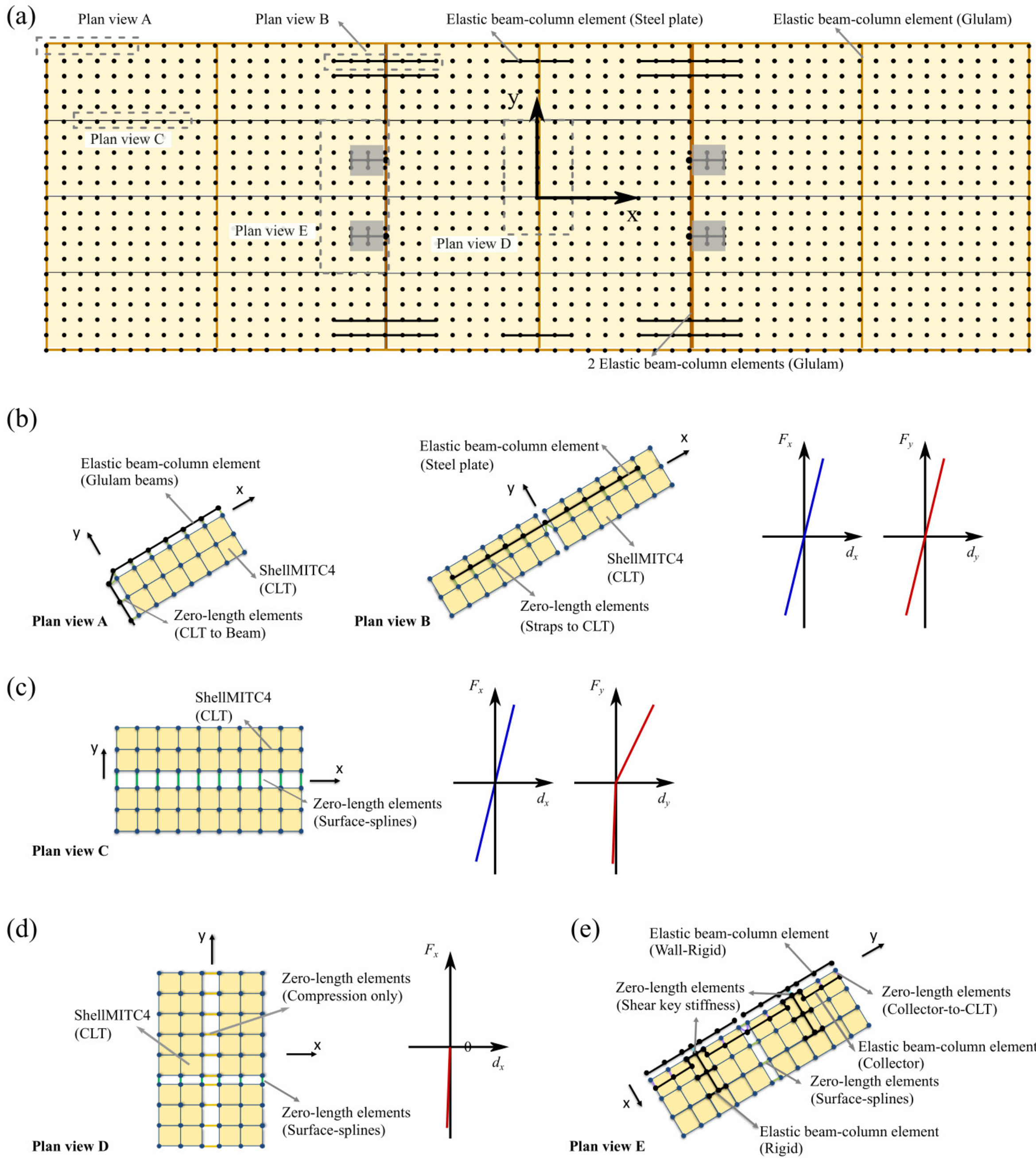

Fig. 4. Finite element model details: (a) Mesh discretization; (b) CLT-to-beam and CLT-to-strap connections; (c) Surface splines connections; (d) CLT-to-CLT connection; (e) Wall-to-diaphragm connection

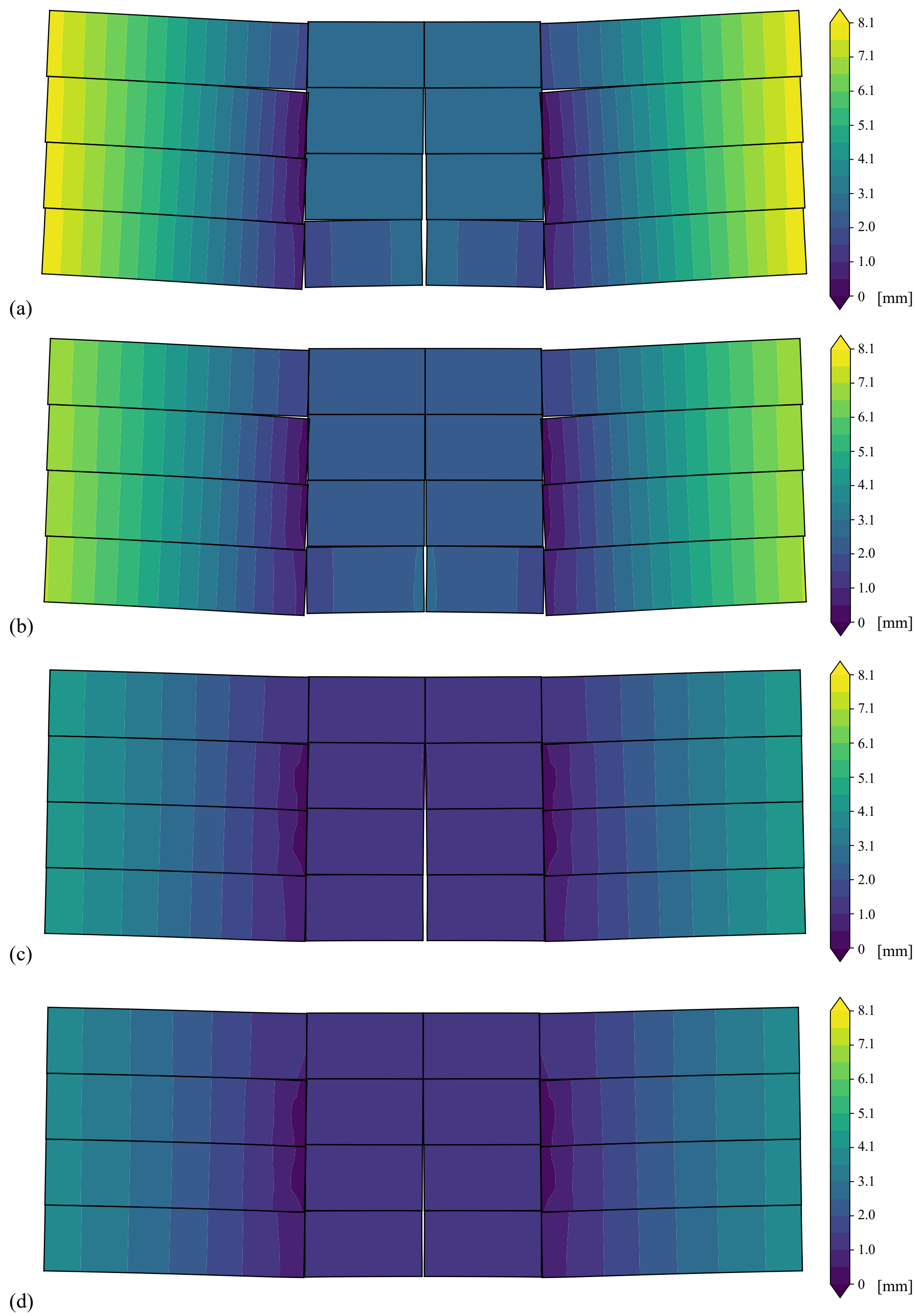

Fig. 5. Deflection diagrams for numerical models: (a) model 1A; (b) model 2A; (c) model 1B; (d) model 2B. Models 1A and 2A are baseline models. Model 1A is based on the numerical modeling approach defined in Section 4. Model 2A is identical to Model 1A except that glulam beams and CLT-to-beam connections are explicitly modeled. Models 1B and 2B are identical to models 1A and 1B, respectively, except that the surface splines are modeled with a stiffness that is 5 times higher than their baseline models.

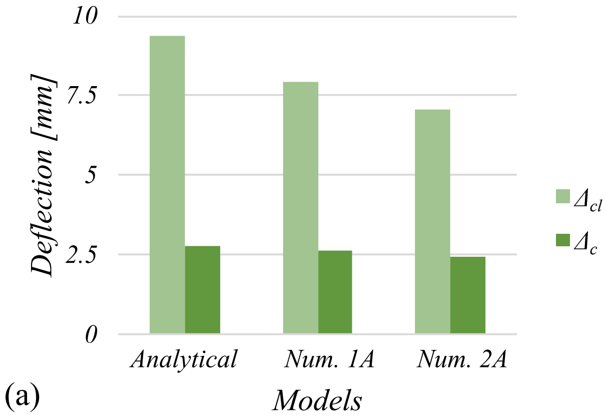

Fig. 6. Deflections computed using the analytical and numerical models when subjected to the seismic loads considered.

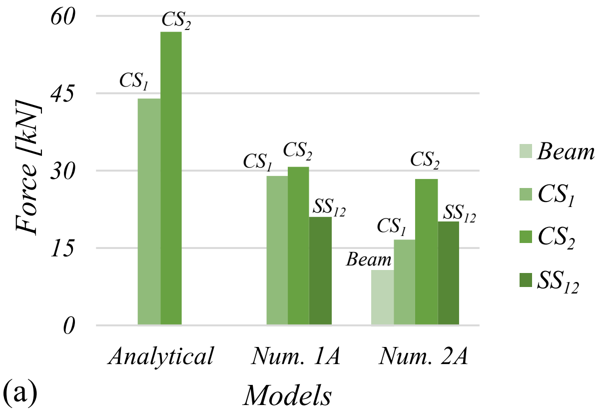

(a)

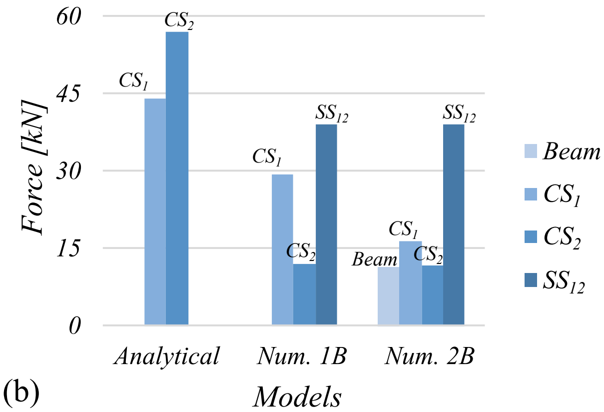

(b)

Fig. 7. Tension chord splices forces for the analytical and numerical models when subjected to the design seismic loads. The diaphragm elements indicated on the graphs can be found in Fig. 2.

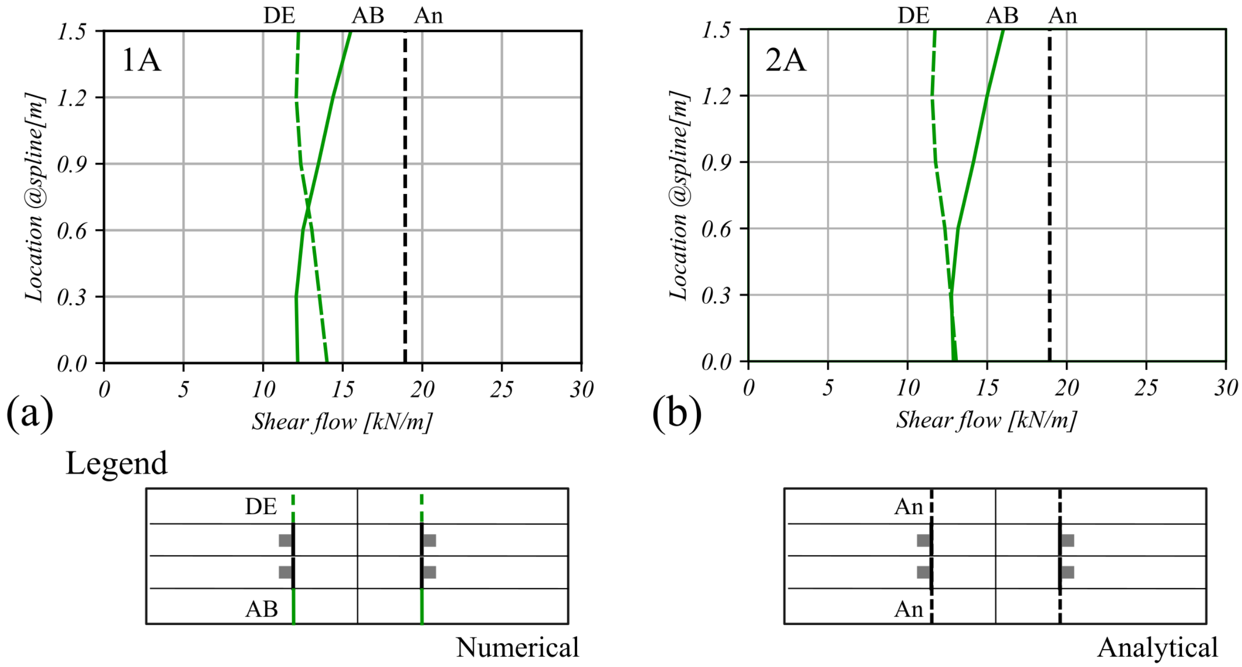

Fig. 8. Shear flow obtained at surface splines aligned with walls: (a) Analytical model vs Numerical model 1A; (b) Analytical model vs Numerical model 2A. Legend: "DE" corresponds to results in numerical models for the spline between gridlines D and E; "AB" corresponds to results in numerical models for the spline between gridlines A and B; "An" corresponds to results in splices shown on the analytical model figure, which are identical for both splices indicated in the drawing.

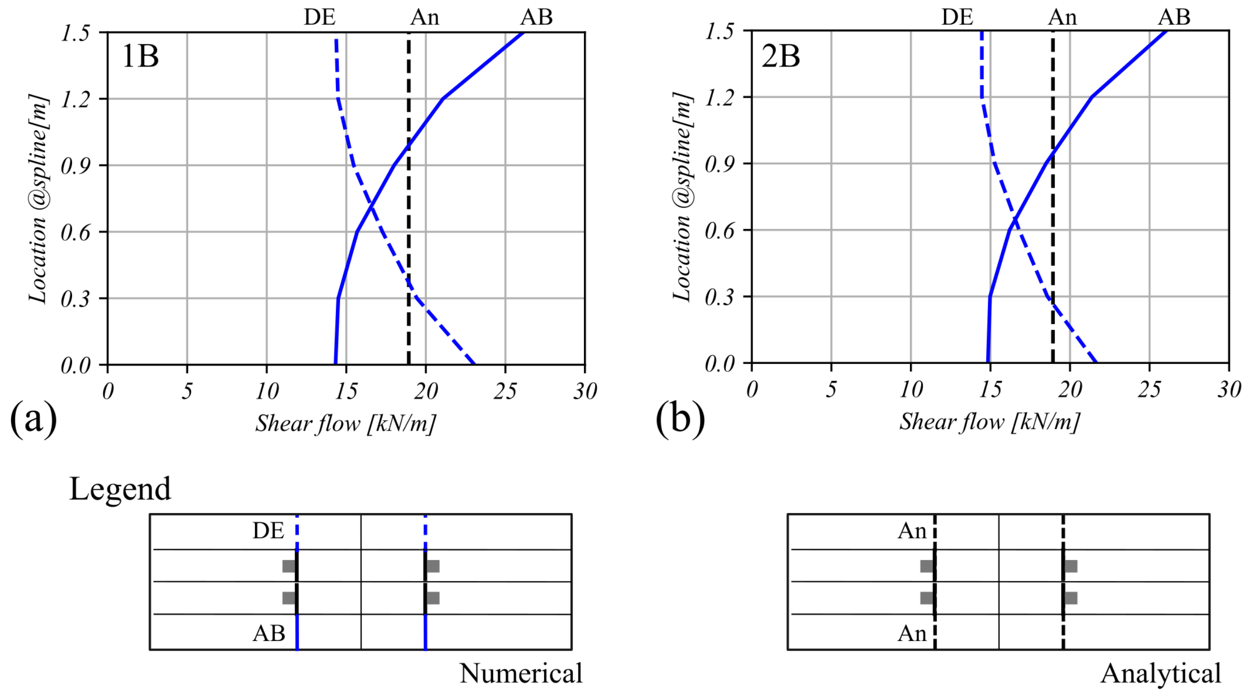

Fig. 9. Shear flow obtained at surface splines aligned with walls: (a) Analytical model vs Numerical model 1B; (b) Analytical model vs Numerical model 2B. Legend: "DE" corresponds to results in numerical models for the spline between gridlines D and E; "AB" corresponds to results in numerical models for the spline between gridlines A and B; "An" corresponds to results in splices shown on the analytical model figure, which are identical for both splices indicated in the drawing.

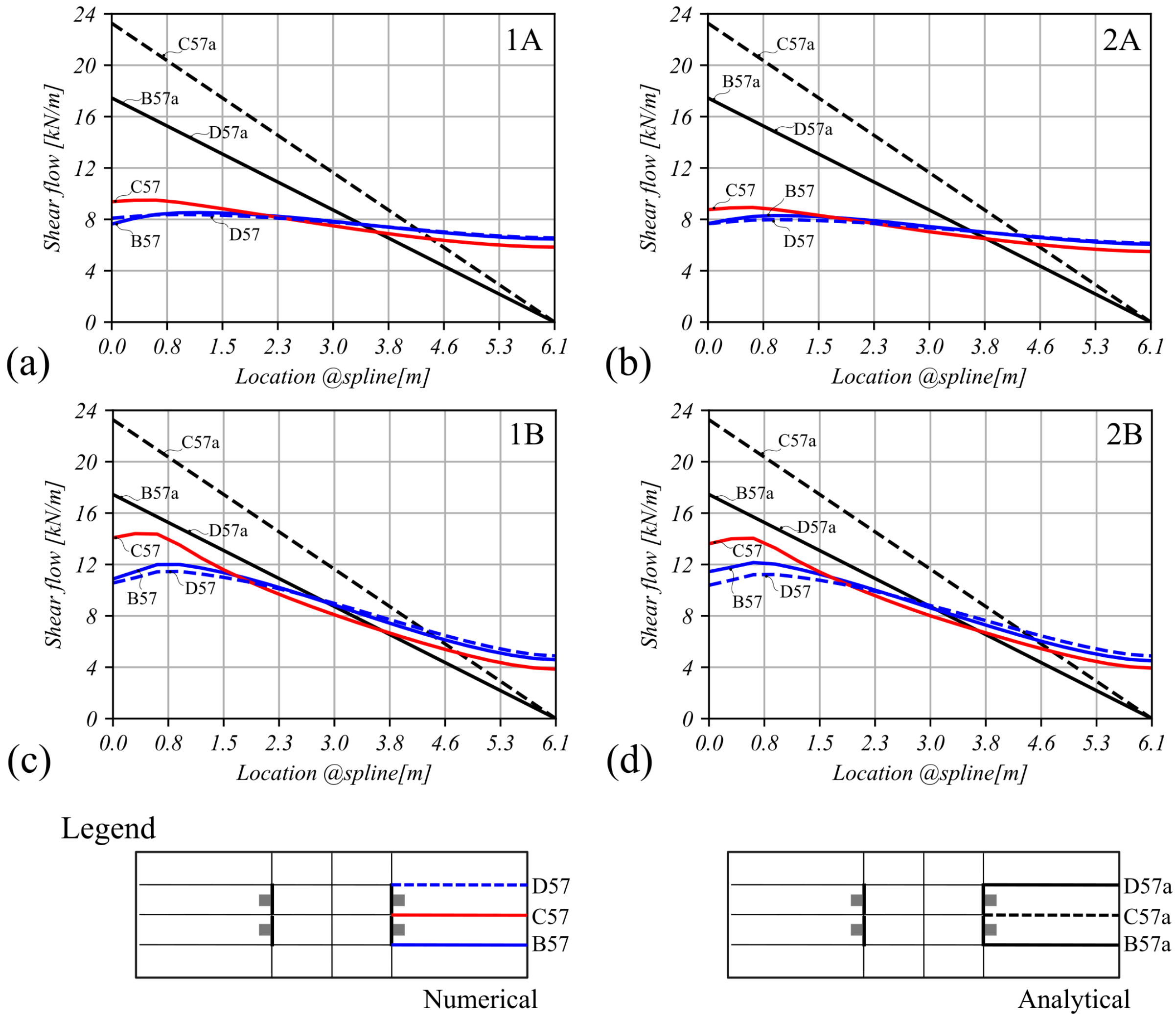

Fig. 10. Shear flow obtained at cantilever surface splines for cases when beams are not modeled ((a) and (c)) and cases in which beams are modeled ((b) and (d)): (a) model 1A, (b) model 2A, (c) (a) model 1B, (d) model 2B.

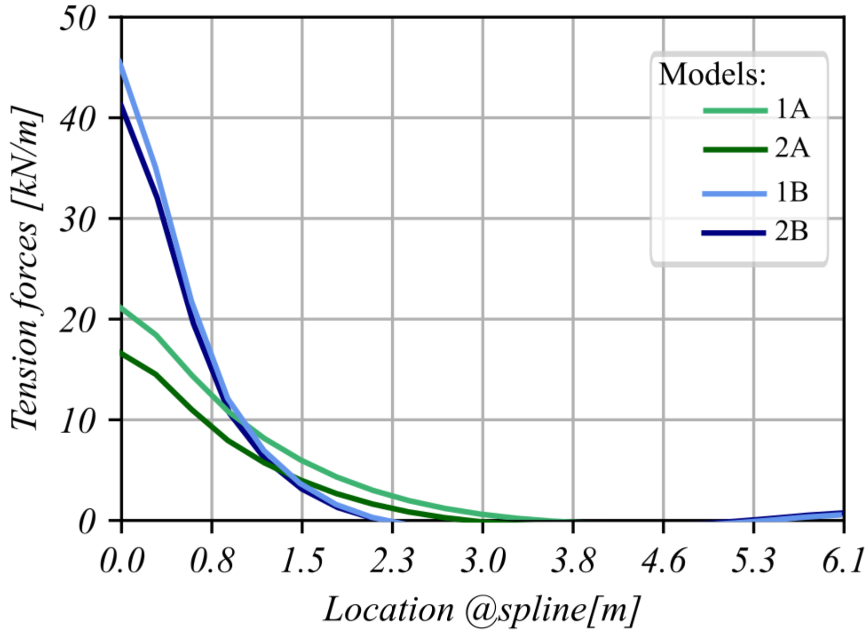

Fig. 11. Sensitivity of tension force at cantilever surface spline SS_3 to the various numerical models developed.

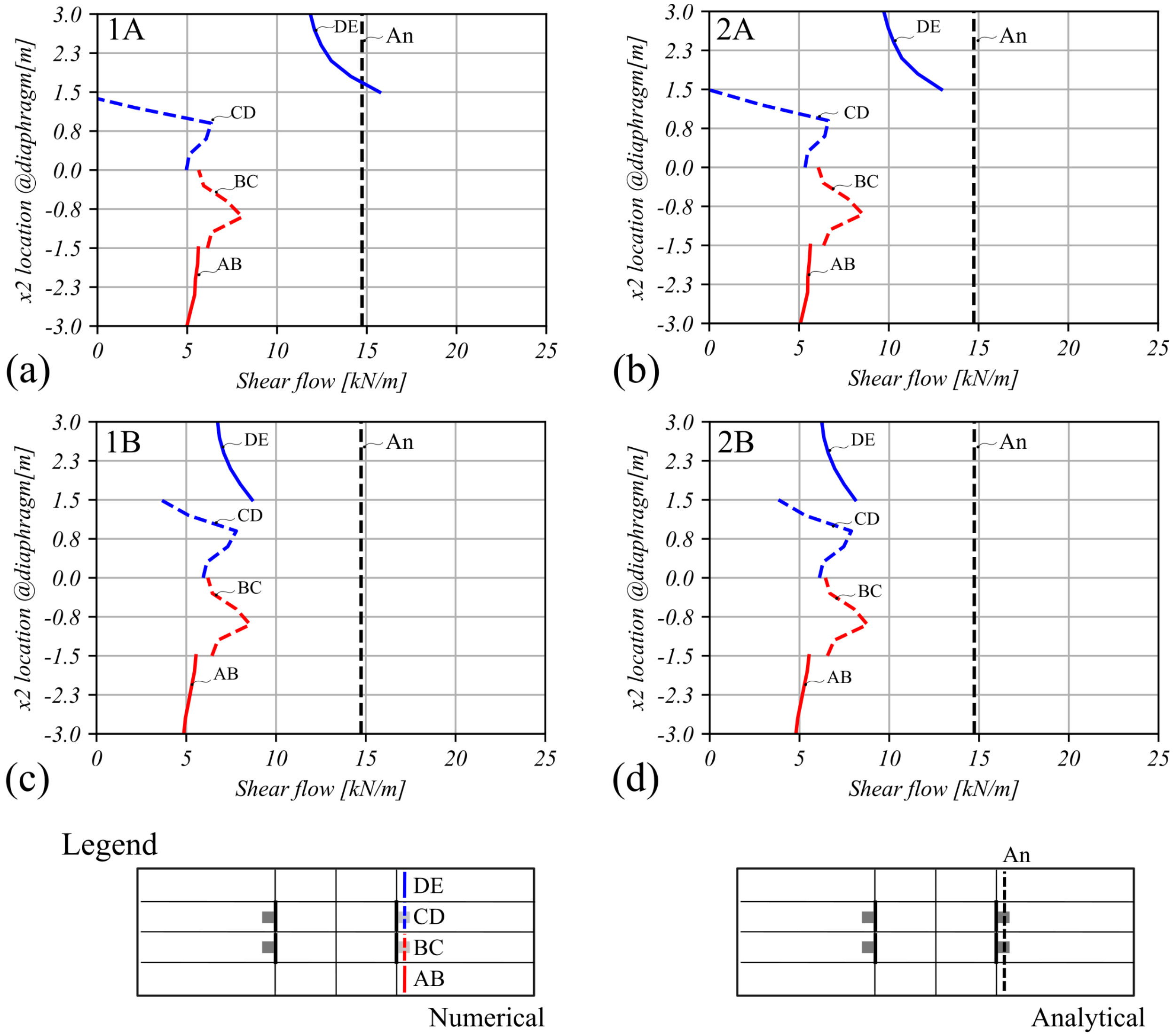

Fig. 12. Shear flow obtained at the collectors for cases when beams are not modeled ((a) and (c)) and cases in which beams are modeled ((b) and (d)): (a) model 1A, (b) model 2A, (c) (a) model 1B, (d) model 2B.

Figure 1a

Click here to access/download;Figure;Figure1a.eps

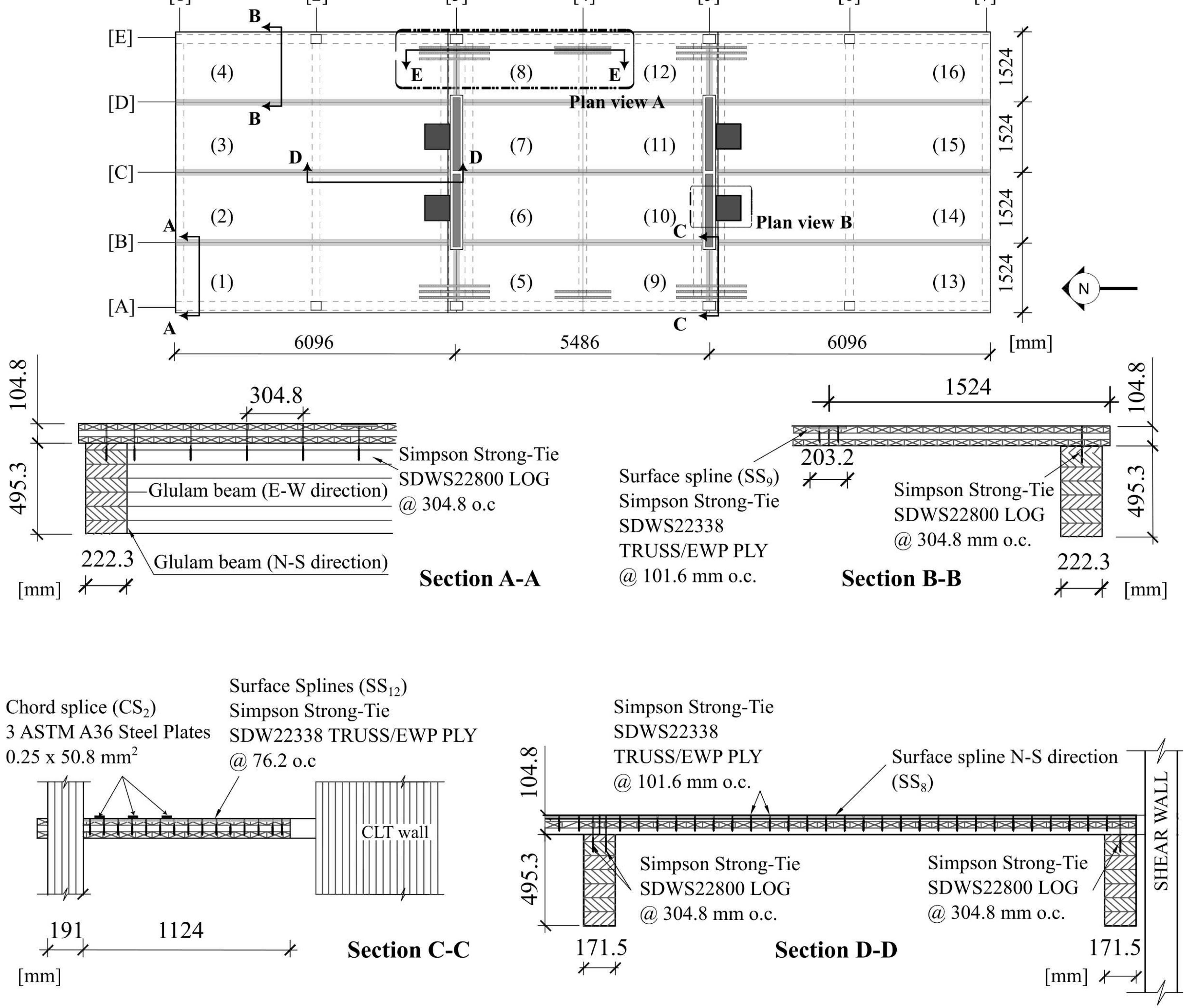

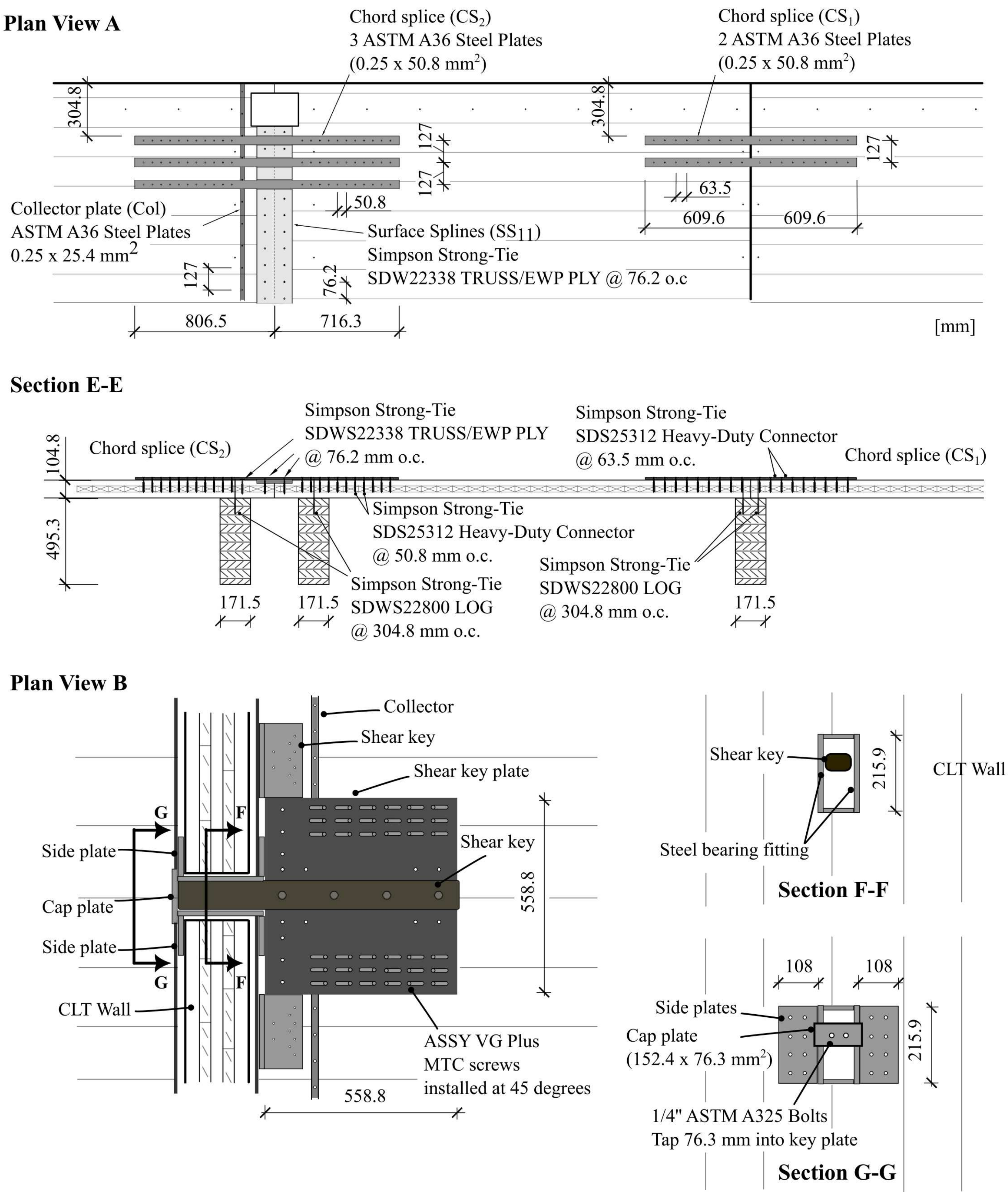
Plan View A
Chord splice (CS_2)
3 ASTM A36 Steel Plates
(0.25 x 50.8 mm^2)
Chord splice (CS_1)
2 ASTM A36 Steel Plates
(0.25 x 50.8 mm^2)
304.8
127
127
304.8
127
63.5
50.8
609.6
609.6
Collector plate (Col)
ASTM A36 Steel Plates
0.25 x 25.4 mm^2
Surface Splines (SS_{11})
Simpson Strong-Tie
SDW22338 TRUSS/EWP PLY @ 76.2 o.c
127
76.2
806.5
716.3
[mm]
Section E-E
Simpson Strong-Tie
SDWS22338 TRUSS/EWP PLY
@ 76.2 mm o.c.
Simpson Strong-Tie
SDS25312 Heavy-Duty Connector
@ 63.5 mm o.c.
104.8
Chord splice (CS_2)
Chord splice (CS_1)
495.3
Simpson Strong-Tie
SDS25312 Heavy-Duty Connector
@ 50.8 mm o.c.
Simpson Strong-Tie
SDWS22800 LOG
@ 304.8 mm o.c.
Simpson Strong-Tie
SDWS22800 LOG
@ 304.8 mm o.c.
171.5
171.5
171.5
Plan View B
Collector
Shear key
Shear key plate
G
F
Side plate
Shear key
Cap plate
558.8
Side plate
G
F
CLT Wall
ASSY VG Plus
MTC screws
installed at 45 degrees
558.8
Shear key
215.9
CLT Wall
Steel bearing fitting
Section F-F
108
108
Side plates
Cap plate
(152.4 x 76.3 mm^2)
215.9
1/4" ASTM A325 Bolts
Tap 76.3 mm into key plate
Section G-G

Figure 2

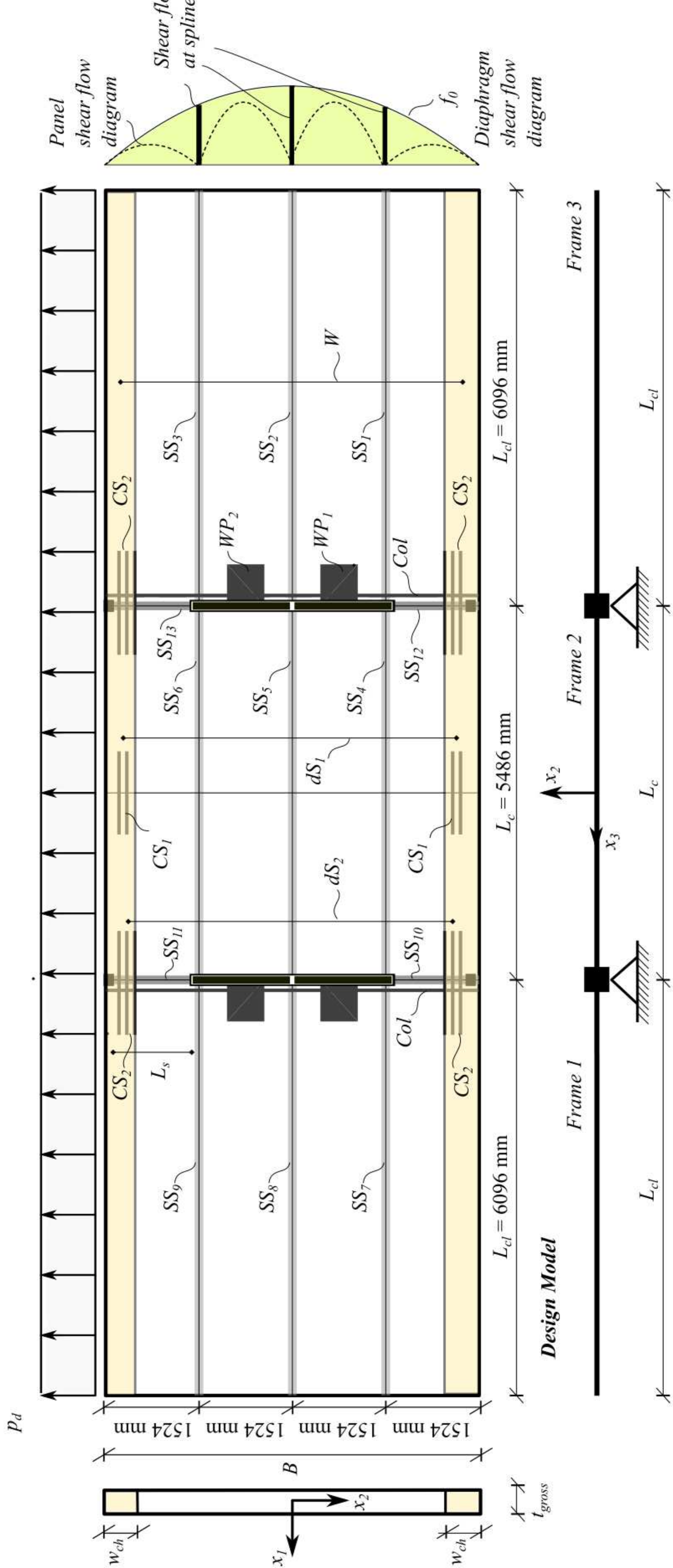

Panel shear flow diagram
Shear flow at splines
f_0
Diaphragm shear flow diagram
p_d
L_{cl} = 6096 mm
L_c = 5486 mm
L_{cl} = 6096 mm
W
dS_1
dS_2
SS_1
SS_2
SS_3
SS_4
SS_5
SS_6
SS_7
SS_8
SS_9
SS_{10}
SS_{11}
SS_{12}
SS_{13}
CS_1
CS_2
WP_1
WP_2
Col
L_s
Frame 1
Frame 2
Frame 3
L_{cl}
L_c
x_1
x_2
x_3
Design Model
1524 mm
1524 mm
1524 mm
1524 mm
B
w_{ch}
t_{gross}

Figure 3 Click here to access/download;Figure;Figure3.eps

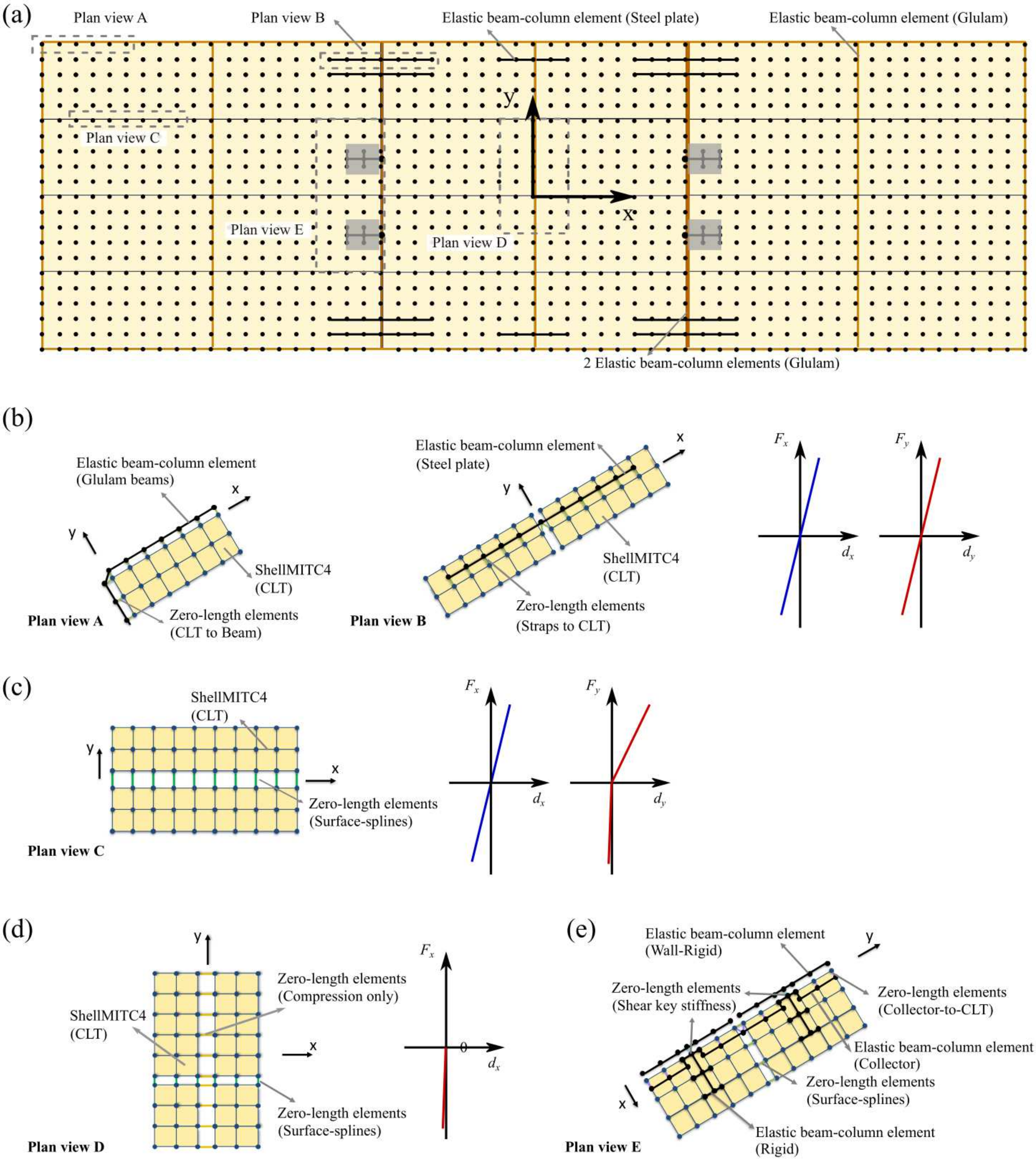

Figure 4

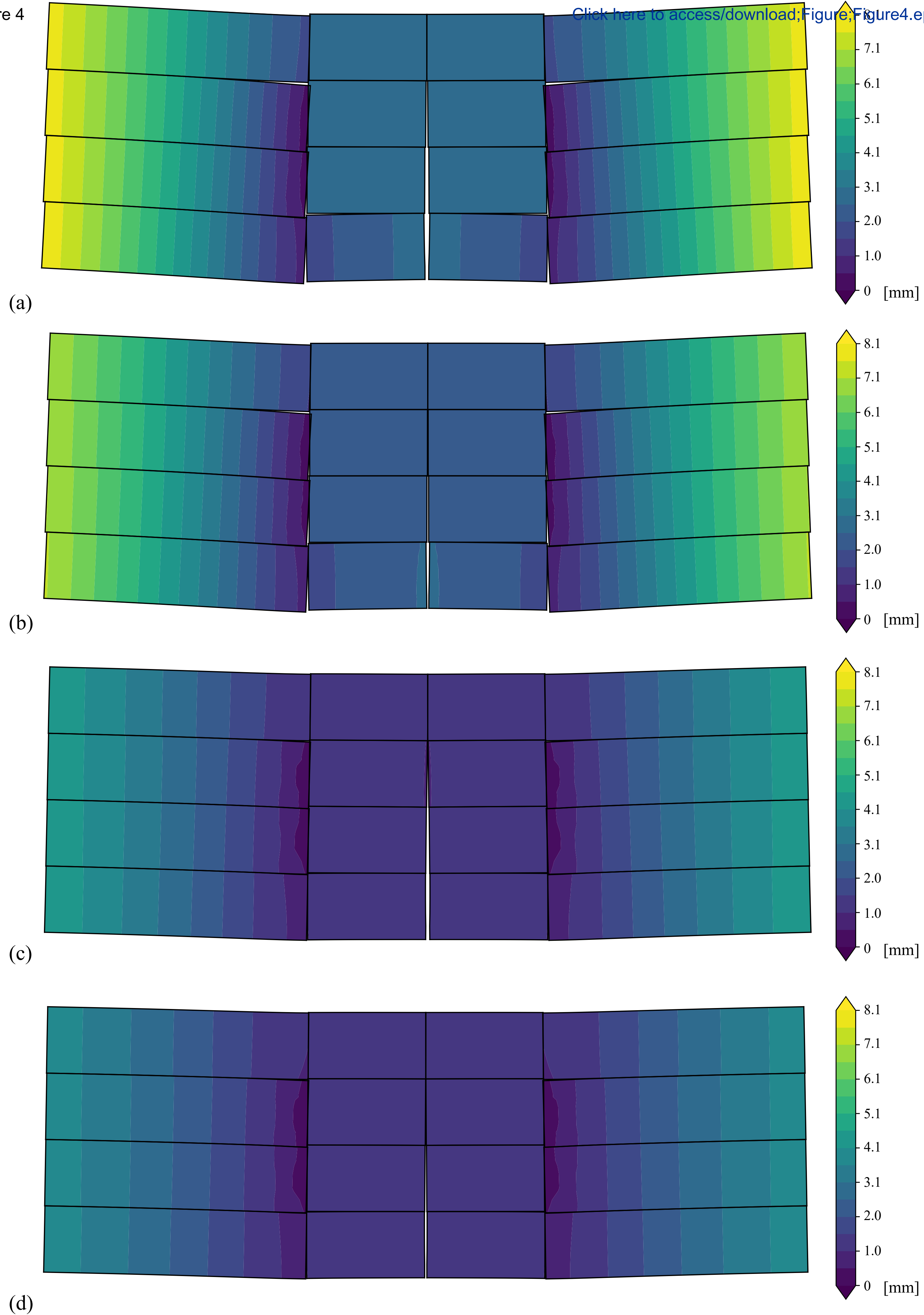

Figure 5

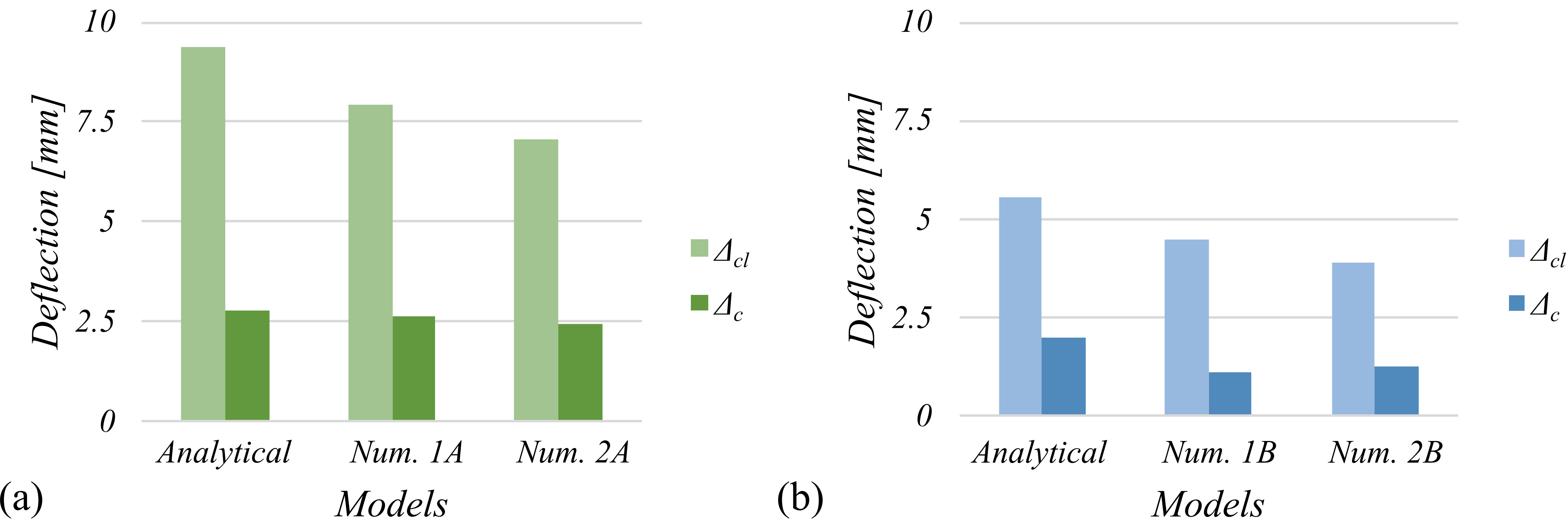

10
7.5
5
2.5
0
Deflection [mm]
Analytical
Num. 1A
Num. 2A
Models
(a)
Δ_{cl}
Δ_c
10
7.5
5
2.5
0
Deflection [mm]
Analytical
Num. 1B
Num. 2B
Models
(b)
Δ_{cl}
Δ_c

Figure 6

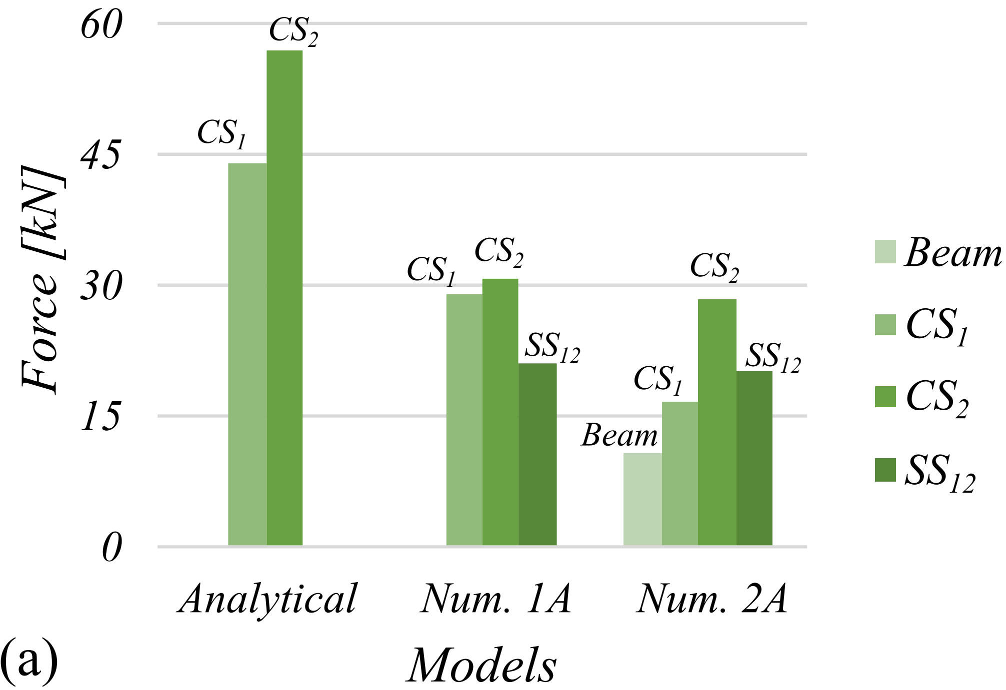
60
45
30
15
0
Force [kN]
CS1
CS2
CS1
CS2
SS12
Beam
CS1
CS2
SS12
Analytical
Num. 1A
Num. 2A
Models
Beam
CS1
CS2
SS12

(a)

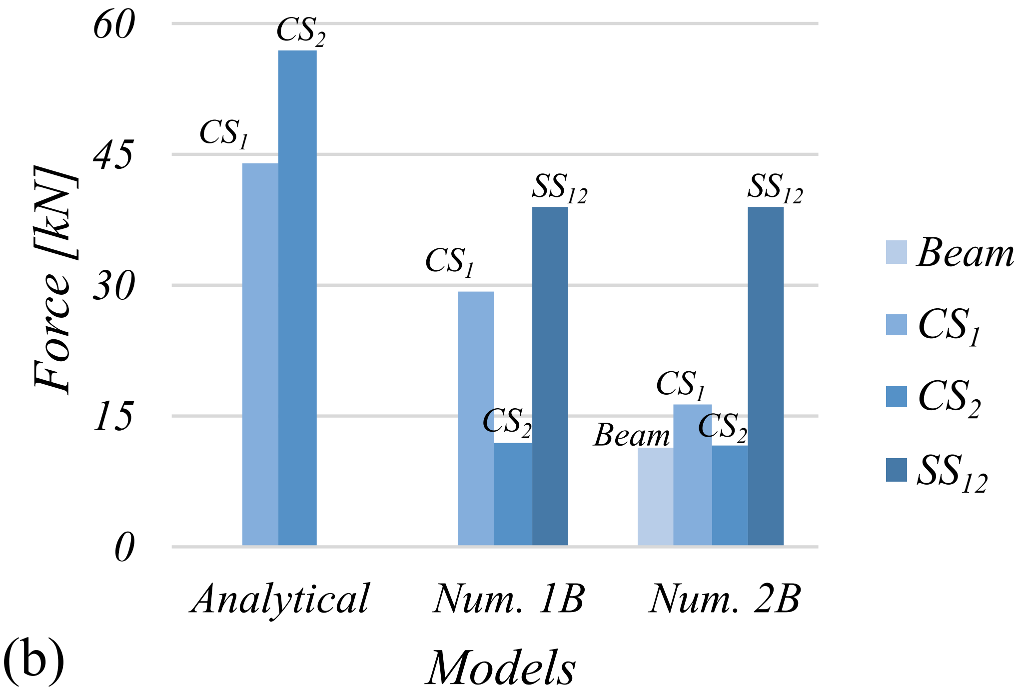
60
45
30
15
0
Force [kN]
CS1
CS2
CS1
CS2
SS12
Beam
CS1
CS2
SS12
Analytical
Num. 1B
Num. 2B
Models
Beam
CS1
CS2
SS12

(b)

Figure 7

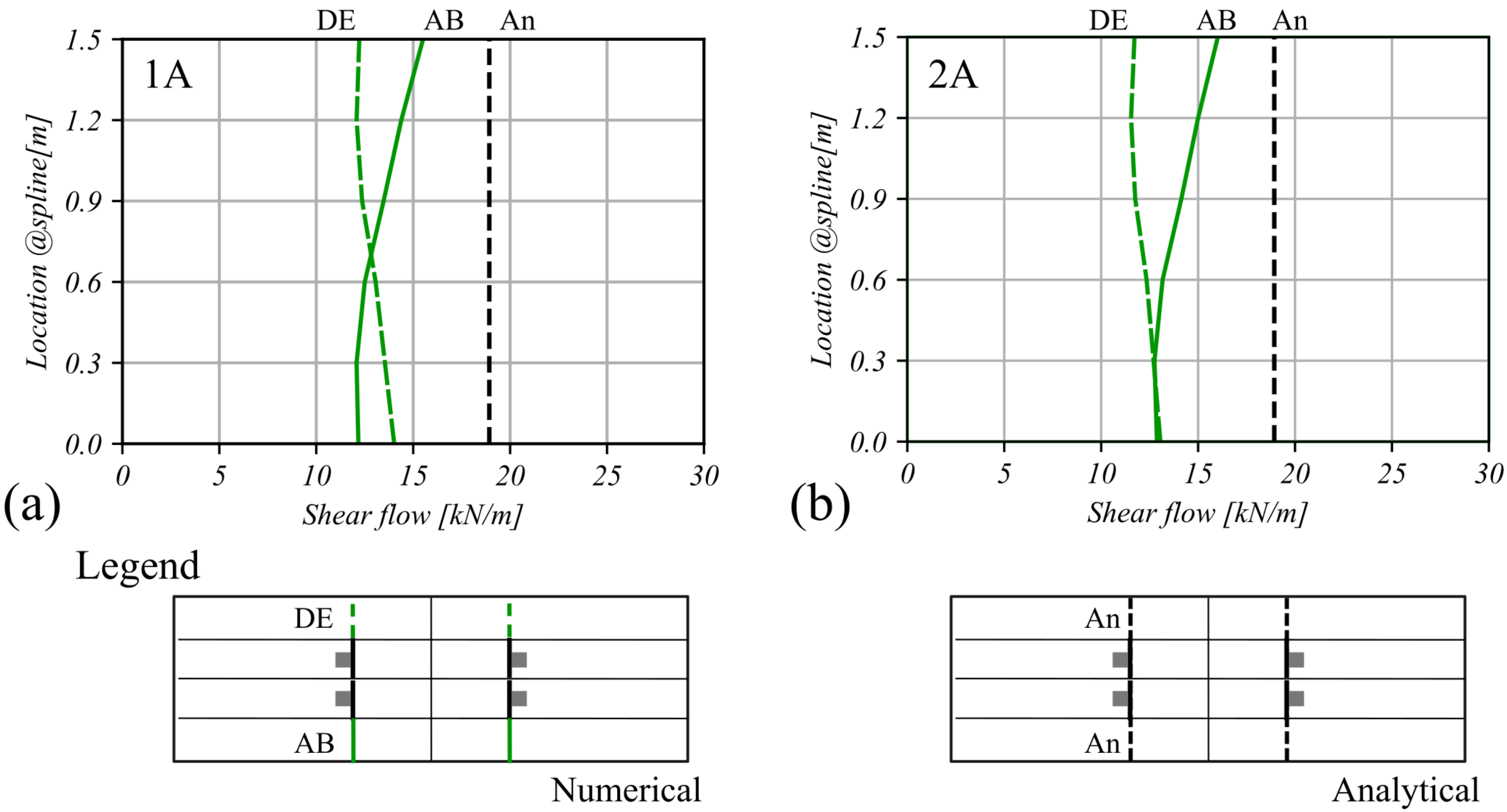
DE
AB
An
1A
1.5
1.2
0.9
0.6
0.3
0.0
Location @spline[m]
0
5
10
15
20
25
30
Shear flow [kN/m]
(a)
DE
AB
An
2A
(b)
Legend
DE
AB
Numerical
An
An
Analytical

Figure 8

Click here to access/download;Figure;Figure8.eps

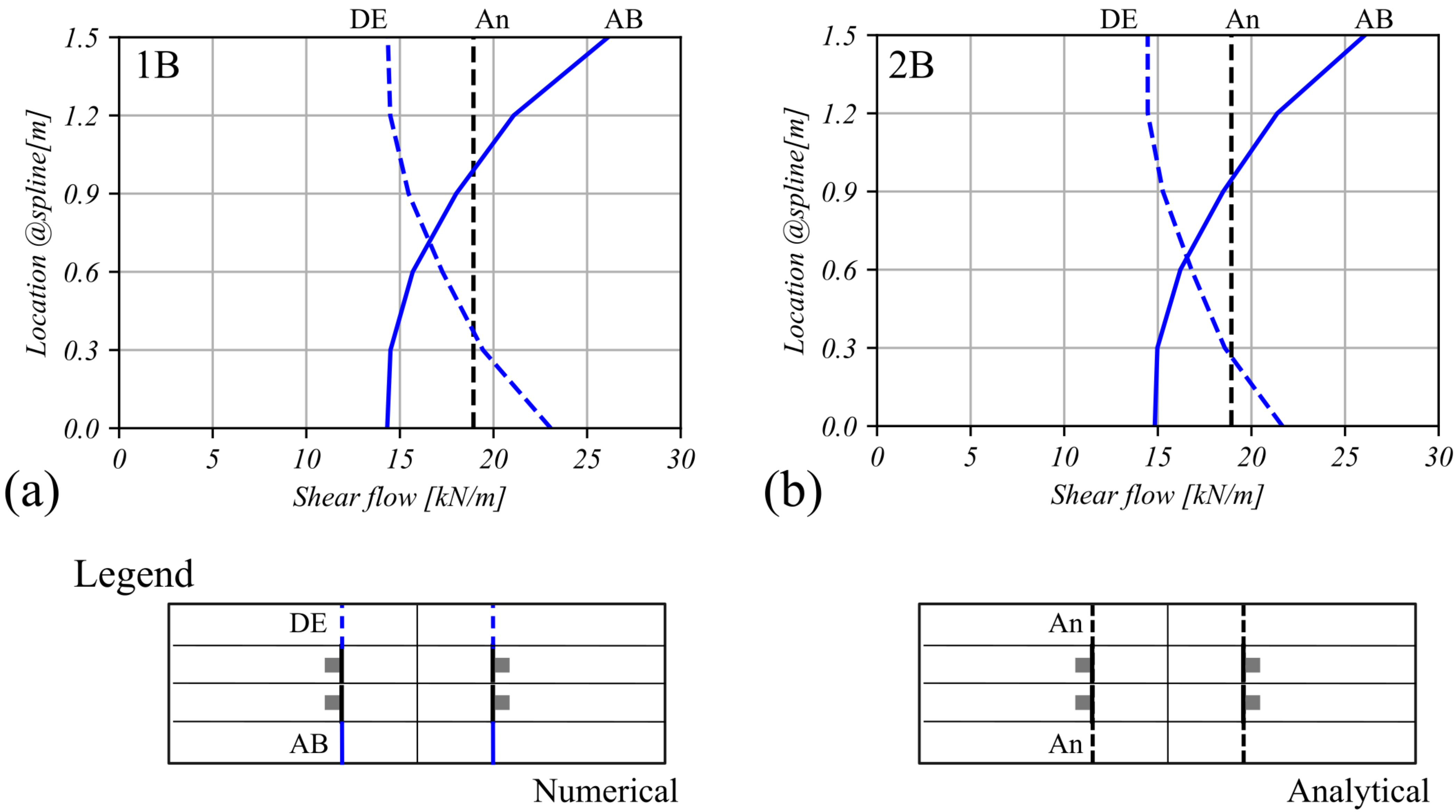

Figure 9

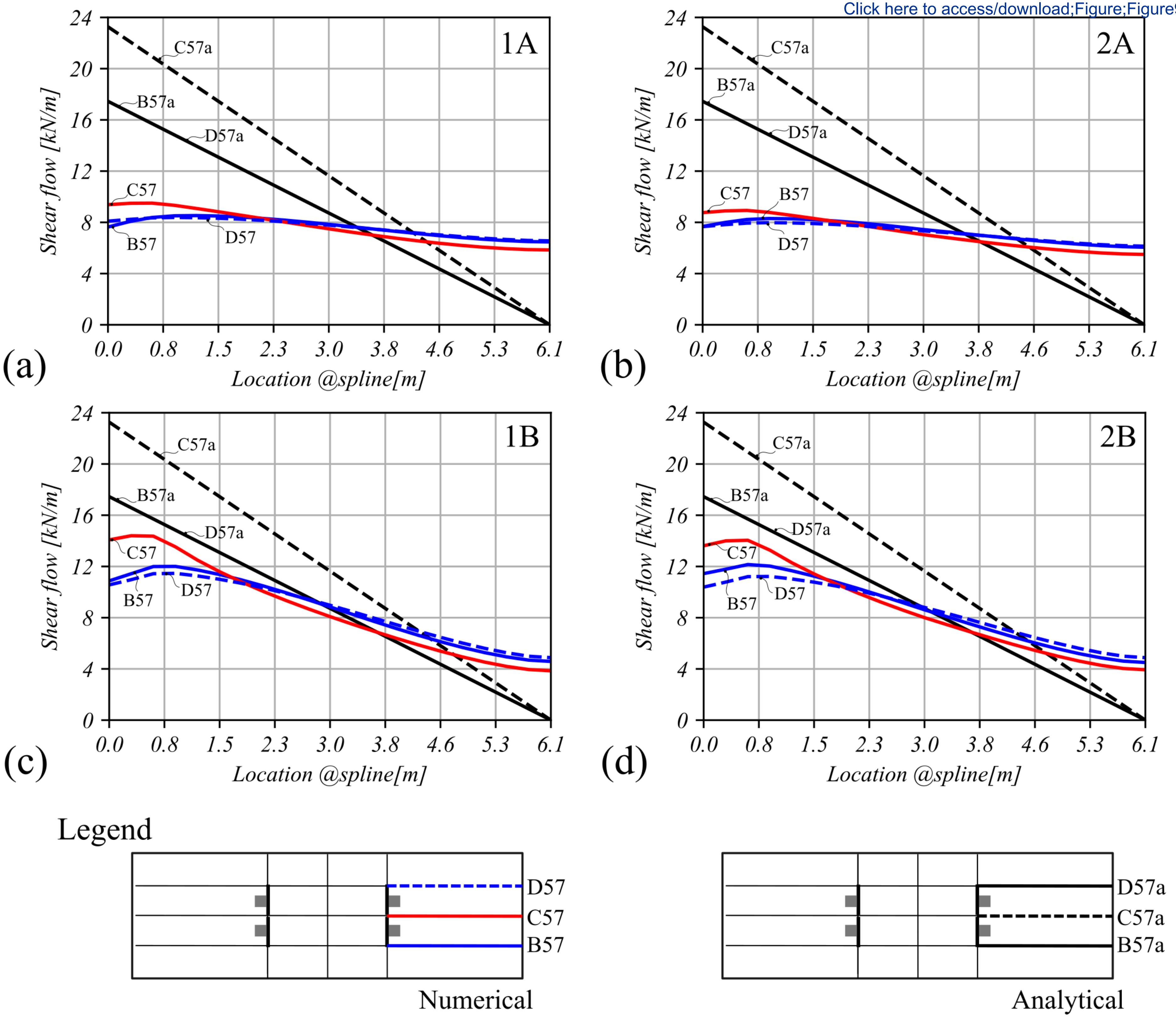
1A
2A
1B
2B
C57a
B57a
D57a
C57
B57
D57
Shear flow [kN/m]
Location @spline[m]
0.0
0.8
1.5
2.3
3.0
3.8
4.6
5.3
6.1
0
4
8
12
16
20
24
(a)
(b)
(c)
(d)
Legend
Numerical
Analytical

Figure 10

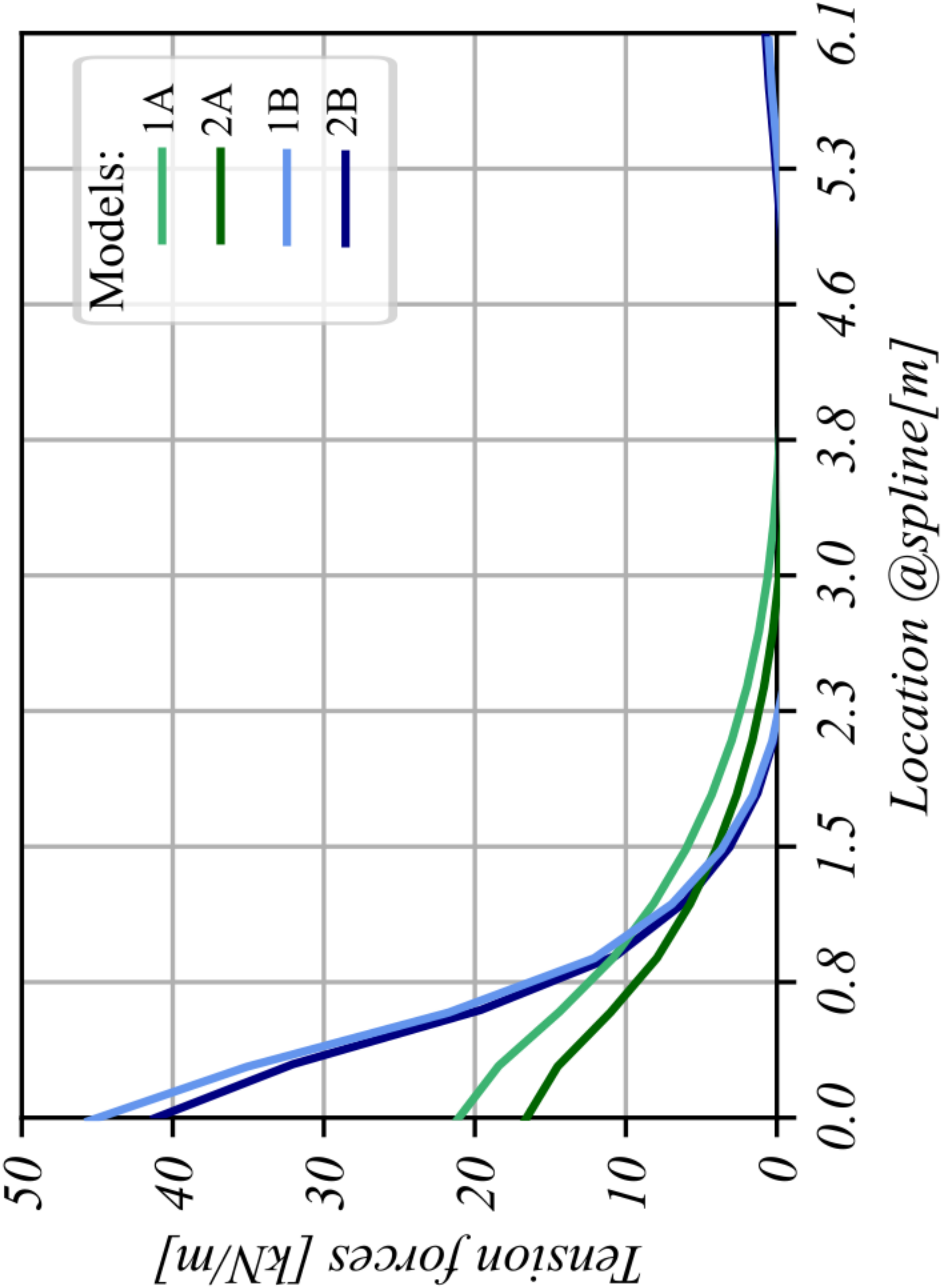
Models:
1A
2A
1B
2B
Tension forces [kN/m]
0
10
20
30
40
50
Location @spline[m]
0.0
0.8
1.5
2.3
3.0
3.8
4.6
5.3
6.1

Figure 11

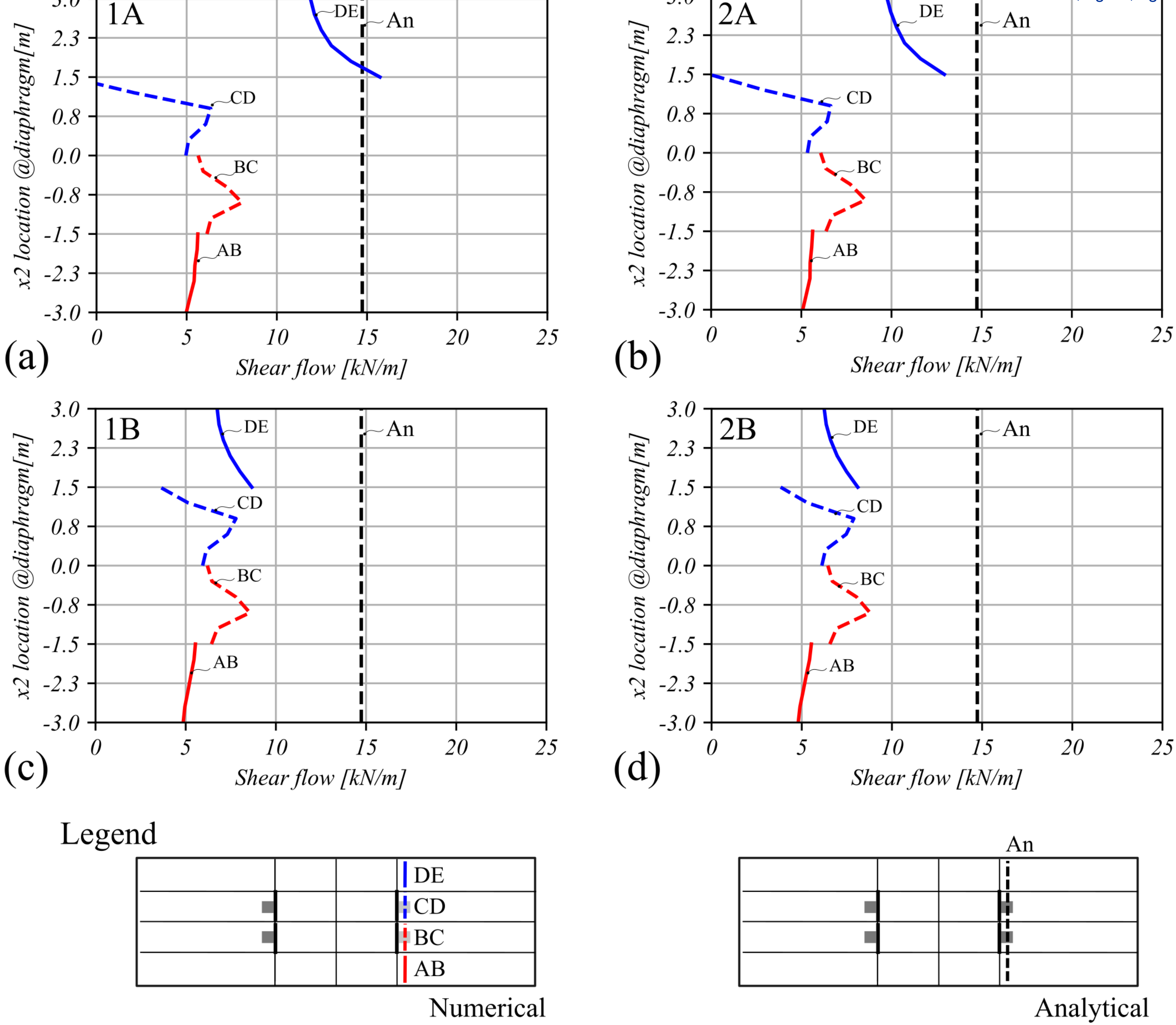
1A
2A
1B
2B
DE
CD
BC
AB
An
x2 location @diaphragm[m]
3.0
2.3
1.5
0.8
0.0
-0.8
-1.5
-2.3
-3.0
0
5
10
15
20
25
Shear flow [kN/m]
(a)
(b)
(c)
(d)
Legend
Numerical
Analytical